Research Square

Preprints are preliminary reports that have not undergone peer review.
They should not be considered conclusive, used to inform clinical practice,
or referenced by the media as validated information.

Influence of dipping heterogeneous layers and contact strength on dyke ascent: Observations from analogue models

Matías Clunes

matias.clunes@uchile.cl

University of Chile

Janine Kavanagh

University of Liverpool

Caitlin Chalk

University of Liverpool

Gloria Arancibia

Pontificia Universidad Católica de Chile

John Browning

University College London

Research Article

Keywords:

Posted Date: November 17th, 2026

DOI: https://doi.org/10.21203/rs.3.rs-11529695/v1

License: This work is licensed under a Creative Commons Attribution 4.0 International License.
Read Full License

Additional Declarations: Competing interest reported. Janine Kavanagh and John Browning are guest editors of the Bulletin of Volcanology special issue "Volcanic and Igneous Plumbing Systems (VIPS): Integrating Observations, Models, and Processes". The authors have no other relevant financial or non-financial interests to disclose.

Influence of dipping heterogeneous layers and contact strength on dyke ascent: Observations from analogue models

Matías Clunes[1, 2*], Janine Kavanagh[3], Caitlin Chalk[3], Gloria Arancibia[4], John Browning[5]

[1]Departamento de Ingeniería de Minas, Facultad de Ciencias Físicas y Matemáticas, Universidad de Chile, Santiago, Chile

[2]Advanced Mining Technology Center (AMTC), Facultad de Ciencias Físicas y Matemáticas, Universidad de Chile, Santiago, Chile

[3]School of Environmental Sciences, University of Liverpool, Liverpool, United Kingdom

[4]Department of Structural and Geotechnical Engineering, Pontificia Universidad Católica de Chile, Macul, Chile

[5]Department of Earth Sciences, University College London, London, United Kingdom

*Corresponding author email address: matias.clunes@uchile.cl

Abstract

Magma intrusions approaching the surface commonly encounter dipping, mechanically heterogeneous layers in folded sequences, composite volcanoes and calderas, yet most models used to interpret volcano deformation assume a homogeneous or horizontally layered crust. In analogue dyke experiments, we injected water into two layers of elastic gelatine solid separated by a 45°-dipping interface, sing polarised light and particle image velocimetry to track the ascent dynamics. The stiffness ratio (E_U/E_L=0.4-2) of the gelatine, the contact strength (weak or strong) between layers, and the lateral offset between the injection point and the interface were varied. A penny-shaped dyke formed, and its geometry, ascent velocity and eruption location changed depending on whether, and at what depth, it intercepted the interface, and what the stiffness contrast was. Contact strength controlled whether the dyke crossed the interface or deflected along it. When interface interception occurred at depth, lateral growth almost stopped, the upper part of the dyke narrowed and ascent rate increased until eruption, independent of contact strength. Deflection occurred only where a weak contact was combined with an offset injection point, for stiffness ratios above and below unity, and caused the eruption site to be displaced laterally. Asymmetric stress and strain fields developed both around a vertical dyke beneath a dipping stiffness contrast, depending on which layer was stiffer, and around dykes deflected near a weak interface. As both configurations produced asymmetric surface displacement, we suggest an asymmetric deformation signal detected in nature may not by itself distinguish between them. Interception of a dipping contact could also appear as a late acceleration of precursory seismicity and deformation, which may be relevant to hazard assessment.

Keywords: *dyke deflection, gelatine experiments, photoelasticity, mechanical layering, vent location, volcano monitoring*

1. Introduction

Magma ascent through the crust is governed by how the propagating fracture, whether a dyke, sill, or inclined sheet, interacts mechanically with the host rock. The stress and strain generated around its tip and walls ultimately determine whether it stalls, deflects, or reaches the surface (Rubin, 1995; Gudmundsson, 2011; Rivalta et al., 2015). These same interactions leave a signature at the surface, where the resulting uplift or subsidence can be inverted to estimate the depth, volume, shape, and orientation of the intrusion (e.g., Okada 1985; Geshi et al., 2020), making ground deformation the most accessible observational link to processes occurring at depth (Sparks, 2003; Segall, 2013; Gudmundsson et al., 2022). Both the propagation mechanics and the surface signals they produce, however, depend on how the mechanical structure of the host crust is represented (e.g., Trasatti et al., 2003; Masterlark, 2007; Maccaferri et al., 2010; Hickey and Gottsmann, 2014). Most models treat the crust as either an elastic half-space with uniform properties (e.g., Mogi, 1958; Dieterich and Decker, 1975; Okada, 1985; Bonaccorso and Davis, 1999; Feigl et al., 2014), or as a sequence of horizontal layers with contrasting stiffness (e.g., Currenti et al., 2007; Manconi et al., 2007; Masterlark, 2007; Long and Grosfils, 2009; Hautmann et al., 2010; Hickey et al. 2015). Both frameworks are convenient simplifications, but neither holds particularly well beneath a volcanic edifice, especially in orogenic settings. The impact of mechanical heterogeneities and dipping rock layers on the inversion of ground displacement data at volcanic centres remains a significant contributor to uncertainties in key model outputs used in hazard assessments, such as intrusion depth, geometry, volume, and trajectory.

Dipping rock layers are ubiquitous across geological settings. Even within well-studied Icelandic rift zones and composite volcanoes, layers are more commonly inclined than horizontal, dipping outward near the surface and becoming inward-dipping at depth, with dips increasing by roughly 1° for every 150 m of burial in some exposed palaeo-rift sequences (Gudmundsson, 2006). Stratovolcano flanks can dip by up to ~40° and are created by the accumulation of inclined beds of lava and pyroclastic material (Gudmundsson, 2012; Grosse et al., 2014), overlying bedrock sequences that are often folded or tilted, as in the Andes, where magmatic sheets intrude folded strata (e.g., González

et al., 2009; Piquer et al., 2015; Tibaldi et al., 2017; Clunes et al., 2021; Martínez et al., 2023). Caldera-forming ring faults represent a further, steeply dipping structural element in which magmatic sheets are known to be captured and deflected as they propagate towards the surface (Browning and Gudmundsson, 2015), and caldera subsidence commonly tilts marginal strata towards the caldera centre (Branney, 1995; Lipman, 1997; Roche et al., 2000), producing additional dipping sequences around the caldera.

As well as complicating deformation inversions in folded volcanic crust, dip angle and the contrast in stiffness between adjacent layers also shape how a magma-filled fracture interacts with a discontinuity and bonding strength between layers adds a further complication that does not act independently of either. Using elastic-mismatch theory, Gudmundsson (2011) showed analytically that a dyke is more likely to deflect into a contact and form a sill when the material toughness of the interface is low relative to that of the adjacent layers, particularly where a stiffer layer overlies a more compliant one, consistent with earlier gelatine experiments in which sills formed only beneath a more rigid upper layer (Kavanagh et al., 2006). Gelatine analogue experiments varying the thermal welding of the interface between layers of similar stiffness later confirmed this experimentally. A strong, welded interface was crossed by the dyke, whereas a weak interface diverted the intrusion laterally to form a sill or a dyke–sill hybrid (Kavanagh et al., 2015, 2017).

Stiffness contrast, independent of bonding strength, can also control dyke velocity and arrest. Analogue experiments using water and salted gelatine varying the elastic mismatch across a horizontal welded interface identified a critical upper-to-lower layer Young's modulus ratio of 2.1±0.6 above which vertical propagation into the overlying layer is halted and showed that a dyke's ascent velocity immediately after crossing the contact remains partly governed by the elastic properties of the layer it has just left (Ritter et al., 2013). Numerical models coupling viscous magma flow with fracture mechanics show that both the trajectory and the opening profile of a propagating dyke change as it crosses a layered interface, and separately, that an inclined or curving trajectory alone produces comparable changes in dyke shape, indicating that geometry, and not only stiffness contrast, exerts an independent control on how a dyke's form evolves as it propagates through a heterogeneous crust (Furst et al., 2023).

When rock layers are tilted or folded rather than horizontal, this leads to additional complexities. Numerical models of a sill propagating through a folded, heterogeneous crustal segment show that mechanically weak contacts promote local rotation of the stress field and favour deflection into an inclined sheet, but this effect is attenuated as the dip of the folded layers steepens (Clunes et al., 2021). Such weak contacts are not necessarily a lithological property; a pre-existing fracture, a joint or, less commonly, a fault favourably oriented relative to the stress field, can similarly be reactivated as a plane of low resistance to opening (Delaney et al., 1986; Ziv et al., 2000). A dipping discontinuity may therefore represent either a lithological boundary or a reactivated pre-existing fracture. For the former, how contact strength interacts with both dip and the stiffness contrast across the interface remains poorly constrained experimentally. Two broad strategies have been used to represent mechanical heterogeneity of this kind in models of the crust: discrete, contrasting layers joined by an explicit interface (the approach taken here), or treating crustal anisotropy as a continuous, transversely isotropic property of an equivalent homogeneous medium, implemented both in gelatine mixed with quartz sand and mica flakes (Giro et al., 2025) and in finite-element models (Clunes et al., 2026). These approaches, however, cannot isolate the dip or mechanical strength of a single discrete interface from the surrounding anisotropic fabric.

Here we address this gap using a set of gelatine analogue experiments in which two layers of gelatine with contrasting stiffness are separated by an interface dipping at 45°, an intermediate dip within the range of layer inclinations found in folded sequences, composite volcanoes and caldera margins. We vary the stiffness contrast between the layers, the strength of the contact between them and the lateral offset between the injection point and the interface, and record the resulting dyke geometry and kinematics, the dyke-induced stress field and the subsurface strain. The mechanical behaviour of the contact between the dipping layers is qualitatively characterised for each experiment. This allows us to evaluate how a dyke-induced stress and strain field is affected by a dipping and mechanically contrasting interface, and to explore the extent to which contact strength modulates this effect. We then discuss how stiffness contrast, contact strength and injection geometry influence dyke deflection and near-surface ascent, and compare the experimental interface with natural dipping discontinuities. Finally, we consider the implications of these results for interpreting ground deformation and other monitoring signals in volcanic settings where dykes ascend through dipping, mechanically heterogeneous sequences.

2. Methods

2.1. Material preparation

To prepare an experiment with two gelatine layers separated by an interface dipping by 45°, 40 litres of gelatine were prepared in two batches with different gelatine concentrations to reach the desired Young's moduli contrast between the layers (Table 1). The gelatine preparation followed the guidelines of Kavanagh et al. (2013), dissolving the required amount of gelatine powder (260 Bloom, 20 mesh, pig-skin gelatine supplied by Gelita UK) in deionised water at approximately 98°C. This mixture was further diluted by cold deionised water using the remaining quantity required to create the final desired concentrations. Lower layer concentrations ranged from 2.5 wt% to 4 wt%, and upper layer concentrations ranged from 2.5 wt% to 5 wt% (Table 1).

To create the dipping interface, the mixture of the lower layer was poured first into a 40×40×40 cm Perspex tank fitted with a hollow metal mould suspended inside it to achieve the required height and position of the interface. The mould was placed, either at the centre of the tank or with an intended offset of 3 cm (Figure 1). The mixture was then left to cool in a fridge at 5°C for 1 or 2 days depending on the desired stiffness to be achieved. The mould was then carefully removed using water at approximately 30°C, and then the mixture of the upper layer was added to the tank over the lower layer following the thermal-welding method of Kavanagh et al. (2015) to create a 'weak' or a 'strong' bond. To create a 'weak' bond, the mixture of the upper layer was added at (or close to) its gel-point temperature (21°C) and when the lower layer had cooled to 5°C. To create a 'strong' bond, the upper gelatine layer was poured over the solidified lower layer when its temperature was ≥28°C. In both cases, the tank was returned to the fridge for additional cooling. Oil was added to the surface of each layer to prevent the formation of a "tough skin" during cooling (Kavanagh et al., 2018). This was removed using a spoon and paper-towel prior to adding the second layer and immediately before measuring the Young's modulus.

For PIV experiments, the same gelatine preparation procedure was followed, but both layers of gelatine were seeded with passive tracer particles coated with Rhodamine-B (e.g., Kavanagh et al., 2015). These fluorescent particles were added first to the cold water and

then to the hot gelatine mixture for each layer prior to it being left to cool, stirring it continuously before being placed in the refrigerator when it reaches 21°C. This step is important to ensure an even distribution of the tracer particles within each solidified gelatine layer.

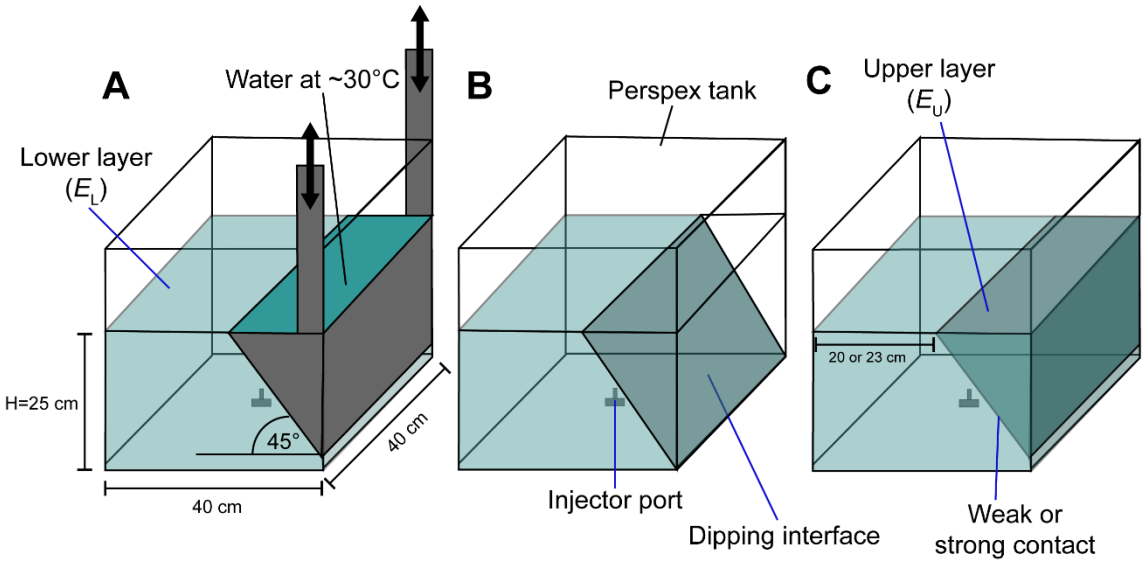


Figure 1: Experimental tank preparation with two layers of gelatine (E_U/E_L) separated by a surface dipping by 45°. Tank dimensions, the location of the injector port and the expected gelatine height (H) are indicated. (A) Experimental tank after pouring the gelatine mixture of the lower layer (E_L). The black arrows indicate that the mould can be lifted for the preparation of the upper layer and for control the final position of the contact between the gelatine layers. (B) Experimental tank before pouring the gelatine mixture of the upper layer (E_U). Experimental tank prior to run an experiment with the measurement of the position of the contact between the layers, being 20 cm at the centre of the tank (D = 0) or ~23 cm (D = 3 cm).

2.2. Material characterisation and scaling

Immediately prior to running an experiment, the Young's modulus of each gelatine layer was measured using the deflection method, applying a load of known mass to the gelatine free surface and measuring the resulting subsidence (Kavanagh et al., 2013). In all the experiments discussed, two layers of gelatine are used and are referred to as E_L for the lower layer and E_U for the upper layer. The ratio of the Young's moduli between these two layers (i.e., the stiffness ratio – E_U/E_L) was always between 0.4 and 2 (Table 1). The contact was qualitatively classified as "strong" or relatively "weak", though it was not possible to directly measure the contact properties. The relative strength was inferred from the preparation temperature and the visually inspected degree of welding, based on the known

198 melting temperature of the gelatine, rather than measured independently. The experimental
199 parameters, the position of the contact between the layers, and the inferred mechanical
200 behaviour of that contact are listed in Table 1.
201
202 Dimensional scaling of the experiments followed the scale factor calculation method
203 described by Kavanagh et al. (2013), based on the buoyancy length $L_b = (\frac{K_c}{\Delta\rho g})^{\frac{2}{3}}$, which
204 defines the characteristic length scale of a fluid-filled fracture propagating through gelatine,
205 where K_c is the fracture toughness of the intruded medium and $\Delta\rho$ is the density contrast
206 between the gelatine and the injected water. Using representative natural values ($K_c =$
207 $10^7 Pa \cdot m\text{^}0.5$), $\Delta\rho = 100\,\frac{kg}{m^3}$, $\rho_{solid} = 2800\,\frac{kg}{m^3}$, and the corresponding experimental values
208 for water injection $K_c = 100\,Pa \cdot m\text{^}0.5$, $\Delta\rho = 100\,\frac{kg}{m^3}$, $\rho_{solid} = 1000\,\frac{kg}{m^3}$), this yields scale
209 factors of $L^* \approx 2 \times 10^{-3}$ for length, $T^* \approx 9 \times 10^{-2}$ for time, $U^* \approx 2 \times 10^{-2}$ for velocity, and
210 $E^* = 2 \times 10^{-6}$ to 2×10^{-5} for stress (Kavanagh et al., 2013). Under this scaling, 1 m of
211 experimental dyke length is equivalent to approximately 500 m in nature, 1 s of experimental
212 time to approximately 11 s in nature. The range in Young's moduli used here (3400–17200
213 Pa; Table 1) are equivalent to natural rock stiffnesses of approximately 0.1–8.5 GPa.
214
215
216
217
218
219
220
221
222
223
224

Table 1: Experimental parameters and variables for each experiment. Experiment codes indicate contact position and behaviour (O = offset, C = centred; W = weak, S = strong), followed by the stiffness ratio (E_U/E_L). The original experiment number is given in brackets. D = Contact distance from the tank centre (offset of the interface relative to the injector, 0 cm = centred). XE_L, XE_U= gelatine concentration (wt%) of the lower and upper layer. H = gelatine height. tE_L, tE_U = cooling time of the lower and upper layer, respectively. Q = injection flux. TE_U = mixing temperature of the upper layer. Contact behaviour = inferred mechanical strength of the contact, based on interface preparation temperature. E_U, E_L = Young's modulus of the upper and lower layer, respectively; E_U/E_L = stiffness ratio between the layers. Monitoring methods used: PIV = Particle Image Velocimetry, Pol = polarised light photoelasticity. Videos of the nine experiments are provided as Supplementary Videos S1–S9, in the order listed here.

Experiment (Reference)	D (cm)	XE_L (wt %)	XE_U (wt %)	H (cm)	tE_L (hr)	tE_U (hr)	Q (m^3/s)	TE_U (°C)	Contact behaviour	E_L (kPa)	E_U (kPa)	E_U/E_L	Monitoring method
OW-0.8 (IL6)	3	2.5	2.5	24	67.7	22.8	3.9 x 10^{-7}	21	Weak	4.1	3.4	0.8	PIV
OW-2A (IL8)	3	3	5	25	68.5	39.5	3.9 x 10^{-7}	21	Weak	8.4	17.2	2	PIV
OW-2B (IL11)	3	3	5	24	92.5	44.5	3.9 x 10^{-7}	21	Weak	5.0	10.1	2	Pol
CW-2 (IL12)	0	3	5	24	93.3	48.8	3.9 x 10^{-7}	21	Weak	6.3	13.1	2	Pol
CW-1.8 (IL9)	0	3	5	25	93.8	41.3	3.9 x 10^{-7}	21	Weak	7.5	13.4	1.8	PIV
OS-0.4 (IL14)	3	4	2.5	25	92.5	42	3.9 x 10^{-7}	36	Strong	13.0	5.7	0.4	Pol
CS-0.5 (IL13)	0	4	5	25	98.3	23.5	3.9 x 10^{-7}	37	Strong	14.2	7.6	0.5	Pol
OS-1.3 (IL4)	3	4	4.5	24	138	43	3.9 x 10^{-7}	36	Strong	10.1	12.8	1.3	Pol
CS-1.8 (IL10)	0	3	5	24	92	47	3.9 x 10^{-7}	36	Strong	8.7	15.7	1.8	Pol

2.3. Dyke injection and imaging methods

Experiments were run by injecting dyed water through a central injector port located at the base of the tank, connected to a peristaltic pump that delivered fluid at a constant volumetric flux $Q = 3.9 \times 10^{-7}\ m^3/s$ (Table 1). A small vertical pre-cut was made in the base of the gelatine to control the orientation of the resulting dyke, ensuring that the tapered edge of the injector was orientated parallel to the crack and that the dyke would propagate parallel to the strike direction of the dipping interface.

2.3.1. Photoelasticity for imaging dyke geometry and induced stress field

Gelatine photoelasticity is used to analyse the evolving strain-induced stress field created by the propagating dyke, by attaching polarising sheets to the outside of the experimental tank on opposite sides, perpendicular to the dyke strike direction (Figure 2A). A light source illuminates the tank from behind, and two HD video cameras record the sub-surface growth of the experimental dyke: one is positioned to record the polarised-light view (HD-1, x-z plane), perpendicular to the strike of the dyke and one is positioned parallel to the strike of the dyke, imaging the plane of the dyke in artificial light (HD-2, y-z plane). A third HD video camera is positioned above the experiment tank to monitor the free-surface of the gelatine (HD-3, x-y plane).

The open-source software Tracker (Version 5.1.5) was used to measure the dyke length, width, and tip position (relative to the injection point) over time. The measurements were made directly on the recordings obtained by cameras HD-1 and HD-2. Since the dimensions of the dyke were measured manually picking its vertical and lateral extent, a positional error of approximately 0.3–0.6 mm is associated with these measurements, corresponding to an uncertainty of ~2–3 pixels given the camera resolution and calibrated field of view (40 cm) for each imaging system (1920 × 1080 px, corresponding to 0.21 mm/pixel for the HD-1/HD-2 cameras used for photoelastic imaging, and 2752 × 2200 px, corresponding to 0.145 mm/pixel for the PIV camera). To exclude the near-injection transient associated with the earliest stage of dyke growth, the dyke parameters are presented only for the uppermost 15 cm of the gelatine (Figure 6), i.e. after the dyke had propagated ~9–10 cm from the injection point. Images obtained from the Tracker recordings were used to observe and describe

variations in the gelatine stress field induced by dyke propagation at specific times during the experiments.

Three dyke parameters were extracted from video tracking: dyke width (the horizontal extent of the dyke measured in the strike-parallel view where the dyke is widest), ascent rate (the rate of vertical advance of the dyke tip, computed from the change in dyke length, i.e., the vertical distance from the injector to the tip, between consecutive tracked frames), and dyke dip (the local inclination of the tip trajectory from horizontal, with 90° corresponding the vertical propagation). Ascent rate and dyke dip were averaged over 1-cm depth intervals. These measurements are illustrated schematically in Figure 2, which also shows the narrowing of the dyke above the interface (necking), described qualitatively in this work.

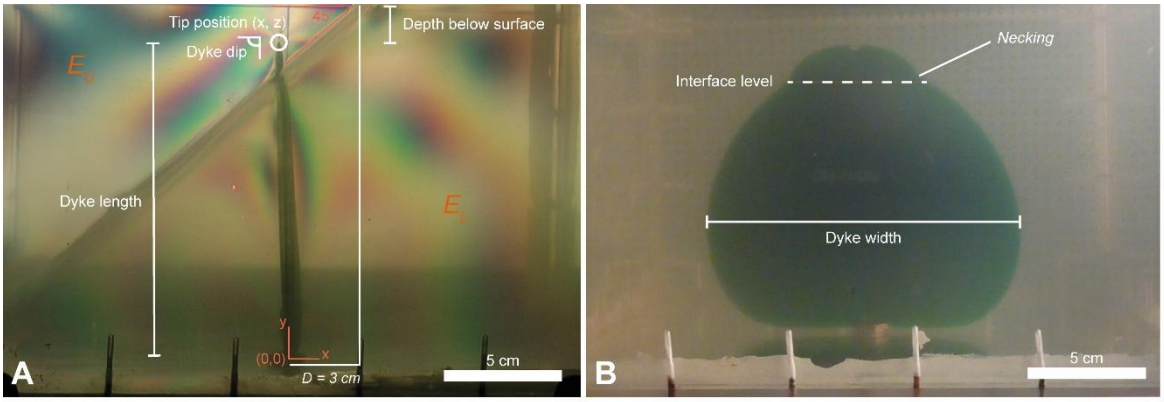


Figure 2: Parameters measured on the gelatine analogue experiments. (A) Strike-perpendicular (photoelastic) view of a dyke propagating through layers of contrasting stiffness (E_U, E_L) separated by a 45°-dipping interface (offset experiment, D = 3 cm). Tip position (x, z) is tracked relative to the origin (0,0) at the injection point. Dyke length, the vertical distance from the injector to the tip, is used to calculate ascent rate, and dyke dip is the local inclination of the trajectory from horizontal (90° = vertical). Depth is measured from the gelatine surface. (B) Strike-parallel view showing dyke width, measured where the dyke is widest. The dashed line marks the interface level. Above it, the dyke forms a narrower lobe (necking).

2.3.2. Laser imaging for dyke-induced subsurface strain measurement

To monitor dyke-induced strain evolution in the layered gelatine, PIV-derived Digital Image Correlation (DIC) was used following the procedure described by Kavanagh et al. (2018). In PIV experiments (Figure 3B), a Class 4 Double Pulse Nd:YAG laser system consisting of a laser head and two LPU1000 power supply units was used. The two beams output from the same exit port through a 25mm convex cylindrical lens and the pulse width was 6 ns with a

303 wavelength of 532 nm. The maximum laser output energy was 2x325 mJ, reducible by
304 increasing the attenuation, set at 40%. The beam was fired through a 3 mm slot to form a
305 vertical sheet aligned with the injector. The laser excites 20-50 μm fluorescent, spherical
306 poly (methyl methacrylate) (PMMA) passive tracer particles with a Rhodamine-B coating,
307 giving peak fluorescence at a wavelength of 590 nm. Images were captured on an Imager
308 SX 6M CCD camera with a Zeiss 50 mm f/1.4 lens with an aperture of f/5.6, with an exposure
309 time of 200 μs and a resolution of 2752 x 2200 pixels. A longpass (550 nm) filter was fitted
310 to the CCD camera to capture only light reflected from the fluorescent particles. Prior to each
311 experiment, a 2D calibration image was obtained by filling the tank with water and aligning
312 a black calibration plate with equally spaced white dots of known size and spacing with the
313 laser beam at the centre of the tank, allowing accurate conversion between pixels and
314 physical distance in post-processing.
315
316 Vector fields were obtained in DaVis (LaVision) by cross-correlation of consecutive images
317 acquired every 10 s, giving a regular grid with a vector spacing of 2.65 mm. Grid points
318 without a valid vector (e.g. within the dyke) were excluded. The vector fields were then post-
319 processed in MATLAB, where the incremental displacement field between consecutive
320 frames was obtained by multiplying the mean of two consecutive velocity fields by the time
321 interval between the frames ($\Delta t = 10\ s$). As displacements are small relative to the vector
322 spacing, incremental strain was calculated from the spatial gradients of this field using
323 Cauchy's infinitesimal strain tensor, following Kavanagh et al. (2018): $\varepsilon_{xx} = \frac{du}{dx}$, $\varepsilon_{yy} = \frac{dv}{dy}$ and
324 $\varepsilon_{xy} = \frac{1}{2}(\frac{du}{dy} + \frac{dv}{dx})$, where x and z are the horizontal and vertical coordinates of the PIV images
325 (Figure 7) and u and v are the corresponding incremental displacements. Gradients were
326 estimated using first-order finite differences on the vector grid.

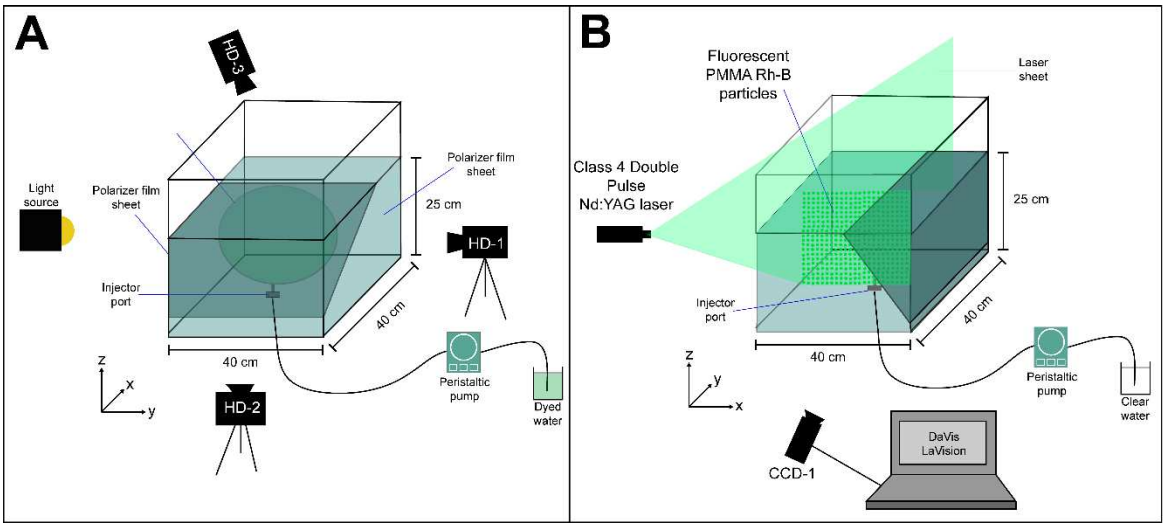


Figure 3: Schematic illustration of the experimental setups, highlighting the camera and laser positions. (A) Experimental setup for the stress field and dyke evolution analysis. (B) Experimental setup for the subsurface strain analysis, in which the green dots represent the fluorescent tracer particles in the laser light.

3. Results

Nine experiments were completed varying the location of the dyke source relative to the interface (O = offset, C = centred), the interface strength (W = weak, S = strong) and the stiffness ratio between the layers (E_U/E_L), either above or below unity. Photoelasticity, video tracking and PIV provide complementary methodologies to capture the main dyke propagation phases and dynamics.

3.1. Central interface

Four experiments were completed with a central inclined interface (CS-0.5, CS-1.8, CW-1.8 and CW-2, Table 1). In all cases, the dyke propagated towards the surface close to vertical as a penny-shaped crack and erupted at the surface without marked deflection (Figure 4 and 6C). A small fissure formed at the surface, parallel to the interface but within the lower layer. Figure 4 compares the two strong contact experiments, in which the stiffness contrast is reversed: CS-0.5 (E_U/E_L = 0.5; Figure 4A-C and 4G-I) and CS-1.8 (E_U/E_L = 1.8; Figure 4D-4F and 4J-L). Three stages of sub-surface stress distribution during dyke propagation are identified: an early stage while the dyke propagates through E_L (Figure 4A and 4D), an intermediate stage as it approaches the interface (Figure 4B and 4E), and a late stage close

to eruption at the surface (Figure 4C and 4F). In both experiments, the dyke remained near-vertical throughout its ascent (Figure 4A-F) and, in the strike-parallel view, grew continuously in width until eruption while keeping a single, rounded outline (Figure 4G-L). At the late stage, the coloured fringes representing the dyke-induced stress field extend above the interface in both experiments, but they are less pronounced within the compliant upper layer of CS-0.5 (Figure 4C) than within the stiff upper layer of CS-1.8, where they are more concentrated, extend downwards along the interface and are markedly more intense (Figure 4F).

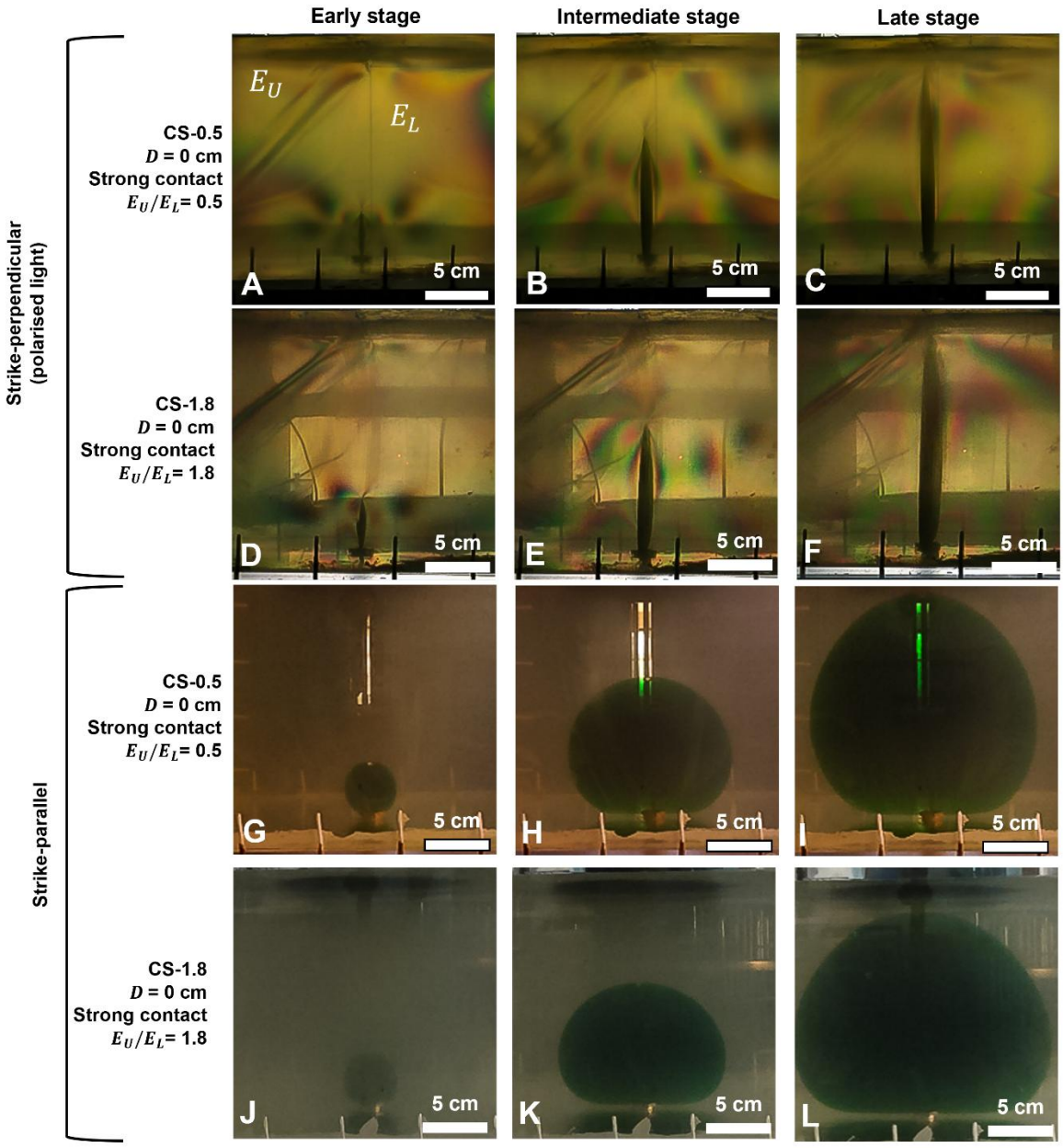


Figure 4: Evolution of dyke geometry and dyke-induced stress field during ascent in the two strong-contact experiments with a centred interface, CS-0.5 (E_U/E_L = 0.5; A–C, G–I) and CS-1.8 (E_U/E_L = 1.8; D–F, J–L). Columns show three stages of ascent: early, while the dyke propagates through the lower layer (tip depth of 20.5 cm in CS-0.5 and 18.1 cm in CS-1.8); intermediate, as the dyke approaches the interface (11.7 and 10.6 cm); and late, close to eruption (3.0 and 1.8 cm). (A–F) Strike-perpendicular view under polarised light; E_U and E_L indicate the upper and lower layers. (G–L) Strike-parallel view.

3.2. Offset interface

Five experiments were completed with an interface offset by 3 cm from the injector, of which two had a stronger contact (OS-0.4 and OS-1.3) and three a weaker contact (OW-0.8, OW-2A and OW-2B; Table 1). Figure 5 compares OW-2B (weak contact, E_U/E_L = 2; Figure 5A–C, 5G–I) and OS-0.4 (strong contact, E_U/E_L = 0.4; Figure 5D-F and 5J–L). OS-1.3 is not shown because its dyke path was deflected by the initial crack at the injection point. In OW-2B, the dyke intruded the weak interface and propagated along it to the surface, erupting as a small fissure within the interface. In OS-0.4, the dyke crossed the strong interface and erupted at the surface, forming a small fissure parallel to the interface but within the upper layer.

In OW-2B, in the early stage (tip depth of 15.8 cm), the coloured fringes were concentrated around the tip within the compliant lower layer and were more intense on the side of the dyke closer to the interface (Figure 5A). In the intermediate stage (tip depth of 7.8 cm), the dyke had a slightly elliptical outline in the strike-parallel view (Figure 5H), and the fringes remained concentrated within the compliant lower layer, mostly on the side of the dyke away from the interface, with only minor fringes in the stiffer upper layer (Figure 5B). In the late stage (tip depth of 2.1 cm), the dyke had reached the interface and was deflected along it (Figure 5C), and the upper part of the dyke had narrowed into a lobe (Figure 5I). At this stage, higher-order fringes (blue to green) remained in the compliant lower layer on the side of the dyke away from the interface, whereas the stiffer upper layer showed a broad, lower-order (red to purple) fringe lobe (Figure 5C). The dyke then propagated along the mechanically weak interface to the surface (Figure 6C). The weak interface was also intruded in OW-2A (E_U/E_L= 2) and OW-0.8 (E_U/E_L = 0.8), which were monitored with PIV (Section 3.4). In both, the dyke was already slightly inclined before reaching the interface (Figure 6C; Section 3.3).

In OS-0.4, in the early stage (tip depth of 16.5 cm), the visibly stressed region was localised at the dyke tip and distributed symmetrically on both sides of the dyke within the lower layer (Figure 5D). In the intermediate stage (tip depth of 9.9 cm), as the dyke approached the interface, it continued to grow vertically with a rounded outline (Figure 5K), but the coloured fringes became asymmetric around the tip and extended across the interface into the compliant upper layer (Figure 5E). In the late stage (tip depth of 6.7 cm), the dyke tip had reached the interface and crossed it without deflection (Figure 5F), and the upper part of the

dyke had narrowed into a lobe (Figure 5L). At this stage, the most extensive and highest-order fringes were in the compliant upper layer around the tip (Figure 5F). The dyke then continued vertically through the upper layer to the surface (Figure 6C).

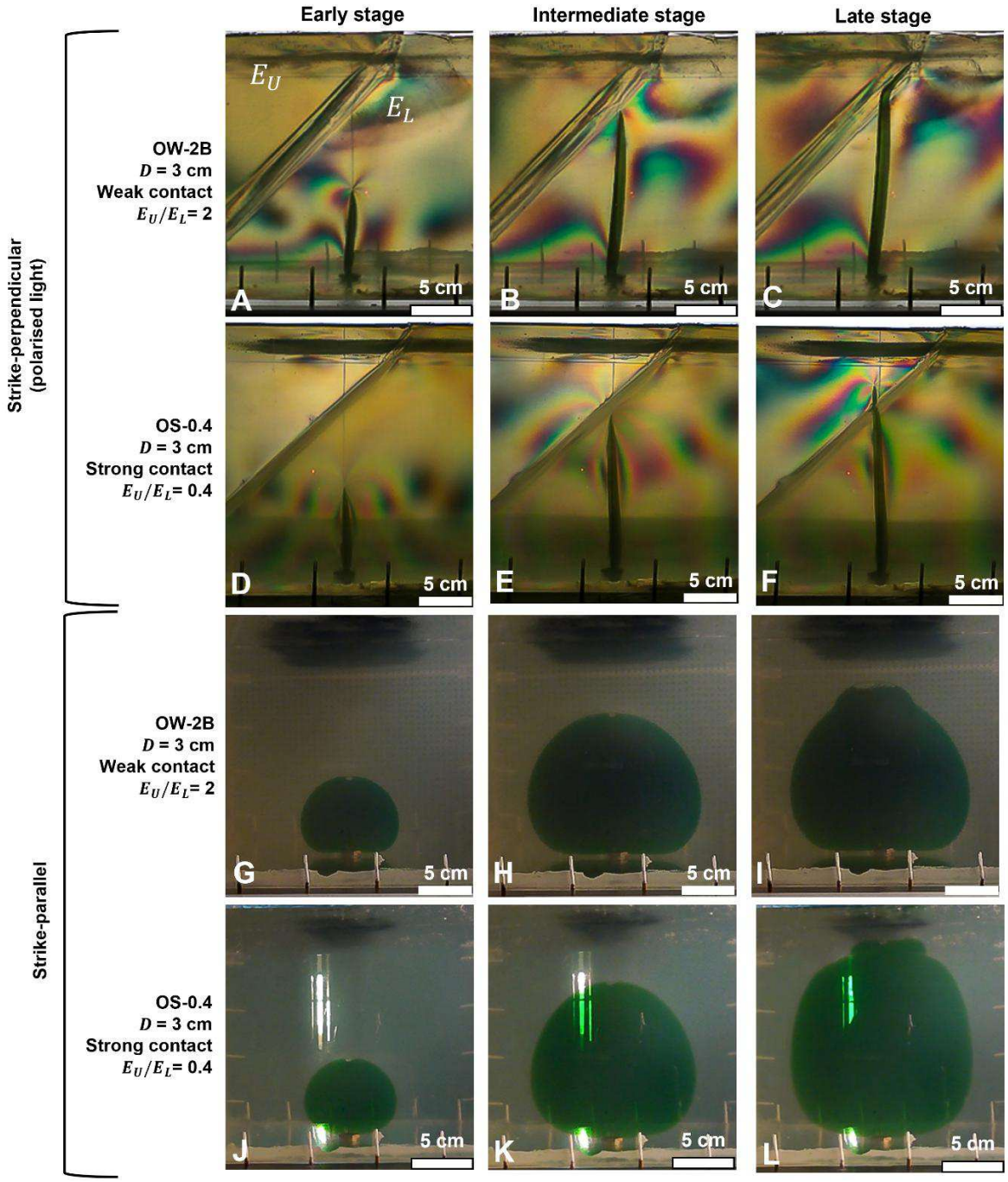


Figure 5: Evolution of dyke geometry and dyke-induced stress field during ascent in two experiments with an offset interface (D = 3 cm), OW-2B (weak contact, E_U/E_L = 2; A–C, G–I) and OS-0.4 (strong contact, E_U/E_L = 0.4; D–F, J–L). (A-F) Strike-perpendicular view under polarised light; E_U and E_L indicate the upper and lower layers (labelled in A). (G-L) Strike-parallel view. Columns show three stages of ascent: early, while the dyke propagates through the lower layer (tip depth of 15.8 cm in OW-2B and 16.5 cm in OW-2B); intermediate, as the dyke approaches the interface (7.8 and 8.8 cm); and late, after the dyke reaches the interface (2.1 and 6.7 cm).

3.3. Kinematic and geometric evolution of the ascending dykes

The photographic observations described above show that both the dyke geometry and the induced stress field change as the dyke approaches and then crosses or follows the layer interface. To quantify these changes across the full experimental set, three dyke parameters (dyke width, ascent rate, and dyke dip, see Figure 2) were extracted from video tracking and compared as the dyke propagates towards the tank surface (Figure 6).

Dyke width (Figure 6A), measured in the strike-parallel view where the dyke is widest, was available for six interface experiments (CW-2, OW-2B, CS-1.8, CS-0.5, OS-0.4, OS-1.3) and for the two non-layered control experiments (SD07 and SD09; Kavanagh et al., 2018). All curves follow a similar trend in the deeper part of the profile, with width increasing from 7.6–9.6 cm at 15 cm depth to 14.1–16.4 cm at 8 cm depth. The curves diverge in the uppermost ~6 cm. In OW-2B and OS-0.4, lateral growth almost stops once the dyke tip reaches the interface (at ~4.5 and ~6.3 cm depth, respectively). From that point to eruption, width increases by less than 0.3 cm, reaching final values of 17.8 and 16.8 cm, and the upper part of the dyke narrows into a lobe (Figures 5I and 5L). In contrast, the other four interface experiments and the two controls continue to widen by 1.7-3.3 cm over the last 6 cm of ascent, reaching final widths of 18.4-20.2 cm and ~21 cm, respectively.

Ascent rate (Figure 6B) is the rate of vertical advance of the dyke tip. Below ~6 cm depth, ascent rate remains low and broadly constant in all nine interface experiments (mostly 0.02–0.04 cm/s; 0.035-0.06 cm/s in OW-0.8), similar to the two non-layered controls (0.03–0.06 cm/s). Within the uppermost ~6 cm, ascent rate increases well above the values of the controls in five of the nine experiments. In OS-0.4 and OW-2B, the increase begins at the depth at which the dyke tip reaches the interface and continues to the surface, reaching 0.18 and 0.68 cm/s, respectively. In OW-2A, CS-1.8 and CW-2, the increase is confined to the uppermost 1–2 cm, with maximum values of 0.66, 0.21 and 0.12 cm/s. In OW-2A, this

increase also begins where the dyke tip reaches the interface, at ~1.5 cm depth. CS-0.5, CW-1.8 and OS-1.3 show no increase beyond the range of the controls (≤0.06 cm/s), and OW-0.8 shows only a slight increase, to 0.07 cm/s.

Dyke dip (Figure 6C) is the local inclination of the tip trajectory from horizontal, with 90° corresponding to vertical propagation. Below ~8 cm depth, all nine dykes propagate close to vertical, with dips of 81–92°. At shallower depths, the three weak-contact experiments with an offset interface deviate markedly from vertical and are deflected along the interface. In OW-2A and OW-0.8, dip begins to decrease several centimetres before the dyke tip reaches the interface. In OW-2A, dip decreases progressively from ~78° at 8 cm depth to ~40° at the surface, approaching the 45° dip of the interface, which the tip reaches at ~1.5 cm depth. In OW-0.8, dip decreases from ~79° at ~6.5 cm depth to ~42° near the surface, similar to OW-2A at the same depths, and the tip reaches the interface close to eruption. In OW-2B, dip decreases from ~88° at 7–8 cm depth to 62–69° above ~6 cm depth. The tip reaches the interface at ~4.5 cm depth, and the dyke is then deflected along it (Figure 5C). In OS-1.3, whose path was affected by the initial crack (Section 3.2), dip decreases gradually from 83° at ~5 cm depth to ~75° at 1.5 cm, and then to ~62° in the uppermost 1 cm. All other experiments (CW-2, CW-1.8, CS-1.8, CS-0.5, OS-0.4) remain within ~12° of vertical (78–93°) throughout the profile, including OS-0.4, in which the dyke crosses the interface without any change in its path.

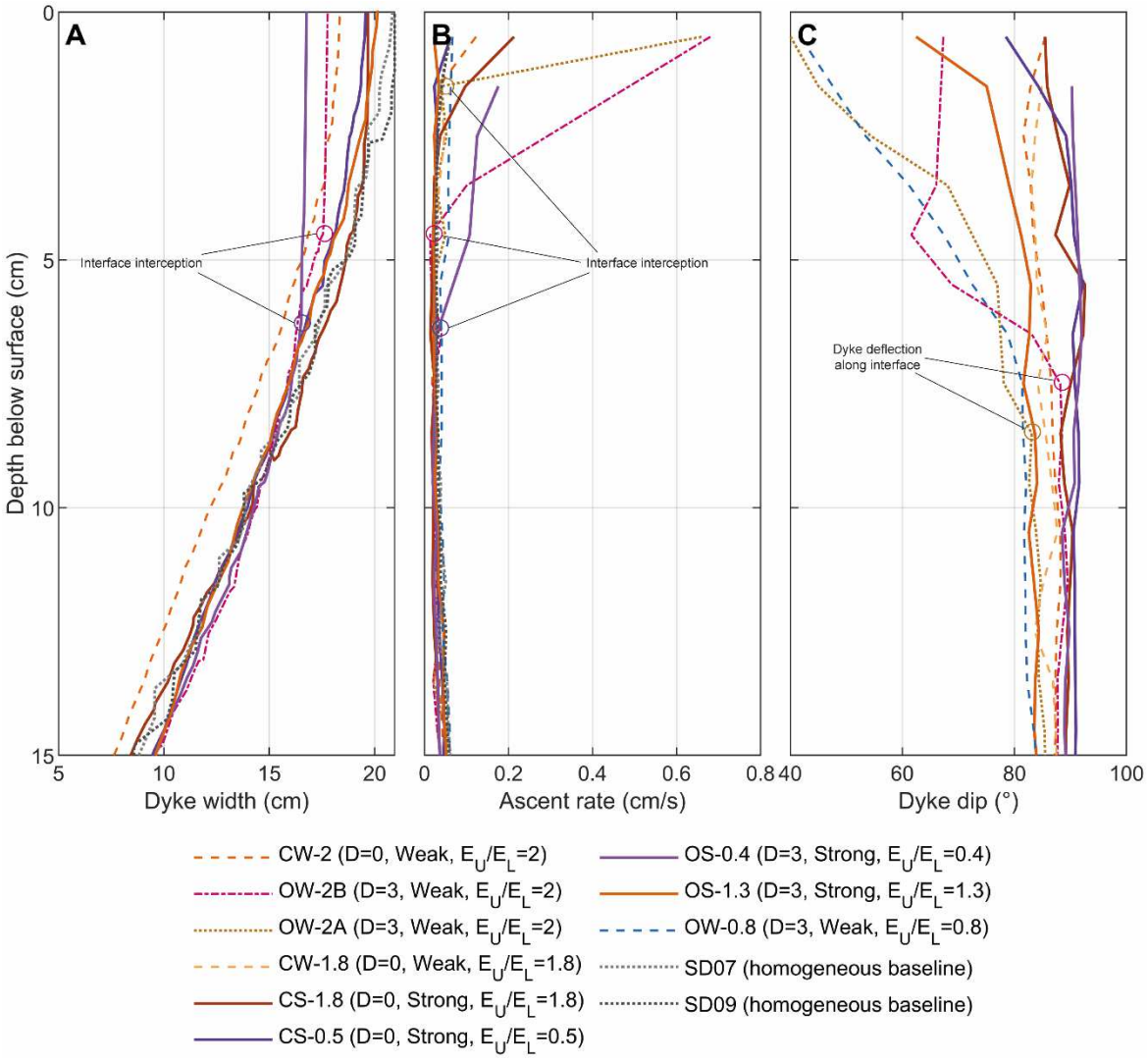


Figure 6: Depth-dependent kinematic and geometric properties of dyke ascent across the full experimental set. (A) Dyke width, measured in the strike-parallel view where the dyke is widest. (B) Ascent rate, computed from the change in dyke length (vertical extent from the injector to the tip) between consecutive frames. (C) Dyke dip, i.e., the local inclination of the dyke tip trajectory from horizontal (90° = vertical). Values in B and C are averaged over 1-cm depth intervals. Warm colours indicate a stiffer upper layer (E_U/E_L > 1) and cool colours a more compliant upper layer (E_U/E_L < 1); solid lines indicate a strong contact and dashed, dash-dotted or dotted lines a weak contact. $D = 3$ cm indicates an injector-interface offset of 3 cm and $D = 0$ cm no offset. Circles mark the depth at which the dyke intercepts the interface (A, B) and the onset of dyke deflection. SD07 and SD09 (grey dotted lines, panels A and B) are non-layered control experiments from Kavanagh et al. (2018).

3.4. Subsurface strain and displacements as a function of stiffness contrast

The PIV-derived DIC results show the subsurface strain and displacement as the dyke ascends and intrudes an offset weak interface underlying a stiffer layer (experiment OW-2A, Figure 7A-I) and a more compliant layer (experiment OW-0.8, Figure 7J-R). The vertical strain component (ε_{yy}) is shown in Supplementary Figure S1. The two experiments share several features, and their dyke paths are similar (Figure 6C).

When the dyke is initially growing through the lower layer, in both experiments the incremental strain is concentrated at the dyke tip, with no incremental strain in the dyke tail region (Figures 7A-C and 7J-L). Displacement vectors show the gelatine being displaced predominantly at the dyke margins, radiating from the tip, with larger lateral than vertical displacement. The largest strain component is horizontal (ε_{xx}), with smaller vertical (ε_{yy}) and shear (ε_{xy}) components. Local positive ε_{xx} occurs at the dyke tip and local negative ε_{xx} adjacent to it. Local positive ε_{yy} occurs just below the dyke tip and local negative ε_{yy} just above it (Figure S1B, H). Local positive shear strain is concentrated at 45° to either side of the dyke tip, with local negative shear strain concentrated on the opposite sides. At this stage the high-strain region in all three components forms a compact, roughly symmetrical patch centred on the dyke tip. In experiment OW-2A, at a tip depth of 17.8 cm (Figure 7A-C), incremental strain ranges from −0.01 to 0.07 for ε_{xx}, -6×10^{-3} to 15×10^{-3} for ε_{yy} (Figure S1), and -15×10^{-3} to 15×10^{-3} for ε_{xy}. In OW-0.8, at a tip depth of 13.5 cm (Figure 7J-L), the strain pattern is similar, with ε_{yy} ranging from -4.0 to 5.8×10^{-3} (Figure S1).

As the dyke approaches the interface between the layers, incremental strain remains concentrated at the growing tip. At this stage, the dyke tip begins to deflect (Figure 6C), and the displacement vectors show a slightly asymmetrical distribution, with lateral displacements larger towards the lower layer than towards the upper layer, and larger than vertical displacements (Figures 7D-F and 7M-O). In OW-2A, at a tip depth of 8.4 cm (Figure 7D-F), the spatial distribution of strain is similar to that of the early stage, but ε_{xx} and ε_{xy} reach lower values (ε_{xx}: -5×10^{-3} to 0.03; ε_{yy}: -5×10^{-3} to 10×10^{-3}; ε_{xy}: -8×10^{-3} to 6×10^{-3}). In OW-0.8, at a shallower tip depth of 6.3 cm (Figure 7M-O), incremental strain is similarly concentrated at the tip but reaches larger values than in OW-2A (ε_{xx}: -12×10^{-3} to 0.05; ε_{yy}: -7×10^{-3} to 17×10^{-3}; ε_{xy}: -10×10^{-3} to 12×10^{-3}).

Shortly before eruption, the dyke tip lies just below the interface and its dip approaches that of the interface (Figure 6C), and the incremental strain is unevenly distributed on either side of the interface. In OW-2A (tip depth of 2.1 cm, Figure 7G-I), incremental strain is concentrated on the side of the dyke tip within the compliant lower layer, with smaller incremental strains along the upper part of the interface. Displacement vectors are also asymmetrical, being larger upwards and towards the stiffer upper layer. In OW-0.8 (tip depth of 2.2 cm, Figure 7P-R), shear strain is distributed within both the upper and lower layers, whereas in OW-2A it remains concentrated within the compliant lower layer (Figure 7I). Unlike the compact, symmetrical incremental strain and displacement observed during dyke propagation at depth, just before eruption the high-strain region in ε_{xx} and ε_{xy} is elongated along the upper part of the dyke, which converges with the interface near the top of the imaged domain, rather than centred on the tip alone. This elongation is less pronounced in OW-0.8 than in OW-2A.

The top of the imaged domain lies ~1-2 cm below the free surface of the gelatine, so the displacement field there is the closest measured counterpart to the deformation produced by the dyke at the surface. While the dyke propagates through the lower layer, displacement near the top of the imaged domain is very small and the strain field is symmetrical about the dyke (Figure 7B, C, K, and L). Asymmetry develops as the dyke approaches the interface and is most pronounced shortly before eruption, when the near-surface strain and displacements are asymmetrical about the vertical projection of the dyke (Figure 7H, I, Q and R). This asymmetry is greater in OW-2A than in OW-0.8, in which the stiffness contrast between the layers is smaller.

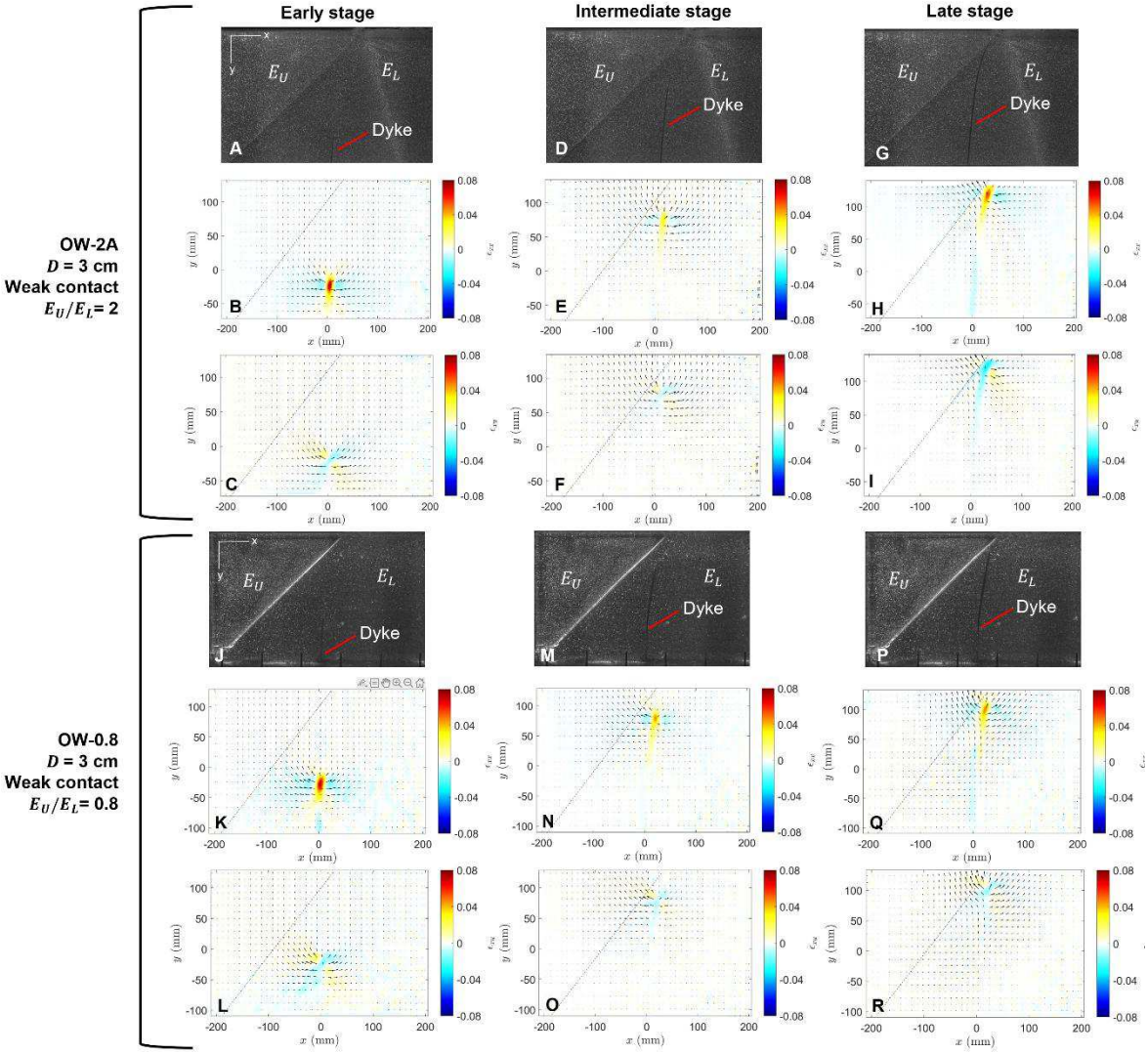


Figure 7: Incremental strain and displacement fields obtained by DIC from PIV images in two experiments with a weak interface offset by 3 cm from the injector, OW-2A (E_U/E_L = 2) and OW-0.8 (E_U/E_L = 0.8), at three stages of ascent (early, intermediate and late). (A, D, G, J, M, P) PIV images showing the position of the dyke and the interface; E_U and E_L indicate the upper and lower layers. (B, E, H, K, N, Q) Horizontal incremental strain (ε_{xx}). (C, F, I, L, O, R) Incremental shear strain (ε_{xy}). Arrows show incremental displacement vectors, and the dotted line marks the trace of the interface.

4. Discussion

4.1. Stiffness contrast, contact strength and injection offset as controls on dyke ascent

The ascent rates presented in Figure 6B suggest that near-surface acceleration may not be adequately explained by contact strength (strong versus weak) alone. In the three offset experiments with a marked acceleration, ascent rate increases from the depth at which the dyke tip intercepts the interface, both with a weak contact and E_U/E_L = 2 (OW-2A and OW-2B, up to 0.66 and 0.68 cm/s) and with a strong contact and E_U/E_L= 0.4 (OS-0.4, up to 0.18 cm/s). In the centred experiments, in which the dyke meets the interface only at the surface, ascent rate increases only within the uppermost 1-2 cm (CS-1.8 and CW-2) or not at all (CS-0.5 and CW-1.8). In OW-2A, interception occurs at ~1.5 cm depth, so its acceleration falls within this same near-surface interval, although it reaches a much higher rate. The two offset experiments with stiffness ratios closest to unity show no marked acceleration, OS-1.3 (E_U/E_L= 1.3), whose path was affected by deflection from the initial crack, and OW-0.8 (E_U/E_L= 0.8), in which the dyke reached the interface only close to eruption. This pattern suggests that whether, and at what depth, the dyke encounters the interface, together with the magnitude of the stiffness contrast across it, may be a primary control on near-surface kinematics. This interpretation rests mainly on OW-2B and OS-0.4, the two experiments in which the dyke intercepts the interface well below the surface, and OW-0.8 is the only weak-contact experiment with a stiffness ratio below unity, so it requires testing with additional experiments.

Contact strength, however, appears to control how the dyke interacts with the interface once it is intercepted, and both modes of interaction are consistent with previous experiments. In OS-0.4, the dyke crosses the strong contact into a more compliant upper layer without any change in its path, and its acceleration agrees with gelatine experiments in which ascent velocity across a horizontal, welded interface increased when the upper layer was more compliant and decreased when it was stiffer (Ritter et al., 2013). In OW-2A and OW-2B, by contrast, the dyke accelerates while propagating along the weak interface rather than into the stiffer upper layer, which may reflect the lower resistance to propagation along a weak interface, as invoked for the acceleration of experimental sills (Kavanagh et al., 2006). The stiffness ratios tested here are below, or within the uncertainty range of, the critical ratio

above which dyke propagation into the upper layer is hindered at a horizontal, welded interface (E_U/E_L = 2.1±0.6; Ritter et al., 2013). Unlike that interface, ours dips at 45°, so the dyke approaches it obliquely, and, in the centred experiments, meets it only at or near the surface. This geometric difference may shift the critical ratio for arrest relative to the horizontal case.

Part of this acceleration could reflect a free-surface effect rather than internal heterogeneity, since fluid-filled fractures in homogeneous gelatine accelerate as they approach the free surface (Rivalta and Dahm, 2006; Gaete et al., 2025), owing to an increase in the stress intensity factor at the tip as the distance to the surface decreases (Rivalta and Dahm, 2006). However, the two non-layered control experiments (SD07, SD09) show comparatively little increase in ascent rate over the same depth interval (up to ~0.06 cm/s; Figure 6B), well below the acceleration documented in OW-2A, OW-2B and OS-0.4 (up to 0.66, 0.68 and 0.18 cm/s, respectively). A free-surface effect alone therefore appears insufficient to account for the magnitude of acceleration observed in these experiments, which supports a contribution from the interaction with the dipping interface.

A related geometric signature is documented in Figure 6A. In OW-2B and OS-0.4, the two experiments with width data in which the dyke reaches the interface before eruption, lateral growth almost stops once the tip reaches the interface, and the part of the dyke that propagates above the interface level forms a lobe markedly narrower than the dyke below it (Figure 5I and 5L). This occurs over the same depth interval as the increase in ascent rate (Figure 6B), as schematically summarised in Figure 8B, whereas the other experiments with width data and the non-layered controls continue to widen until eruption (Figures 4G-L and 6A). Under a constant injection flux, a halt in lateral growth concentrates growth in the vertical direction, so the narrowing and the acceleration are likely to be two expressions of the same process rather than independent observations. Because this occurs despite contrasting contact strength (weak in OW-2B, strong in OS-0.4), stiffness ratios on opposite sides of unity, and contrasting propagation paths (deflected along the interface in OW-2B but near-vertical in OS-0.4), it appears to be linked to the interception of the interface itself. A narrower upper part was also reported in gelatine experiments with a horizontal, welded interface, in which the dyke first propagated laterally at the interface and then pierced it, forming a narrower “bell” on top of an “anvil” (Ritter et al., 2013). In those experiments, however, the anvil became narrower as the upper layer became more compliant and

627 disappeared once it was more compliant than the lower layer, the dyke then widening into a
628 “mushroom” shape. In our experiments, by contrast, lateral growth stops at the interface
629 level instead of spreading along it, ascent accelerates, and narrowing occurs for stiffness
630 contrasts in both directions, which may reflect the 45° dip of the interface or, in OW-2B,
631 propagation along the interface rather than across it.
632
633 Contact strength, in turn, appears to control whether the dyke deflects. A marked deflection
634 occurs only in the three experiments that combine a weak contact with an offset interface,
635 in which dip decreases to ~40° (OW-2A, OW-0.8) or 62–69° (OW-2B) near the surface
636 (Figure 6C). By contrast, the dyke remains within ~12° of vertical in the centred weak-contact
637 experiments (CW-2, CW-1.8) and in the strong-contact experiments, including OS-0.4,
638 which crosses the interface without any change in its path. The only exception is OS-1.3,
639 whose shallow deflection is attributed to the initial crack. Since all these dykes approach the
640 same free surface, a free-surface effect alone cannot account for the deflection, and the
641 dyke in comparable homogeneous gelatine experiments propagated within ±10° of vertical
642 (Kavanagh et al., 2018). Deflection also occurs for stiffness ratios on both sides of unity
643 (E_U/E_L = 2 and 0.8), and OW-0.8 reaches a near-surface dip similar to that of OW-2A. In the
644 material-toughness mechanism of Gudmundsson (2011), based on the elastic-mismatch
645 analysis of He and Hutchinson (1989), deflection is favoured by a stiffer upper layer, but it
646 can also occur between layers of similar stiffness if the toughness of the contact is
647 sufficiently low, less than ~26% of that of the upper layer when both layers have equal
648 stiffness. Deflection in OW-0.8, in which the layers have similar stiffness (E_U/E_L = 0.8), is
649 therefore consistent with this mechanism if the weak contact had such a low toughness,
650 although it differs from early gelatine experiments in which sills formed only beneath a more
651 rigid upper layer (Kavanagh et al., 2006). It also agrees with later gelatine experiments in
652 which sills and dyke–sill hybrids formed at weak horizontal interfaces between layers of
653 equal stiffness, the type of intrusion being controlled by the fracture toughness of the
654 interface relative to that of the gelatine (Kavanagh et al., 2017), and with numerical models
655 of hydraulic fractures intersecting natural fractures oriented at 45°, in which a weakly
656 cemented natural fracture diverts the hydraulic fracture whereas a strongly cemented one
657 does not affect its propagation (e.g., Taleghani et al., 2018). In OW-2A and OW-0.8, dip
658 begins to decrease several centimetres before the tip intercepts the interface (Figure 6B,
659 C). Both dykes were already slightly inclined in the lower layer (81–85°), as in OS-1.3, whose
660 path was affected by the initial crack, so part of this inclination may be inherited from the

initial crack. The subsequent decrease in dip is, however, much larger than in OS-1.3 (53–54° at 2–3 cm depth, compared with ~77° in OS-1.3) and occurs only with a weak contact. Deflection ahead of the interface is consistent with Cook–Gordon debonding, in which a weak contact opens under the dyke-parallel tensile stress ahead of the tip, a mechanism expected to operate mainly at shallow depths (Gudmundsson, 2011). The contact was not monitored ahead of the tip, however, so we cannot confirm that it opened before the dyke reached it.

The stiffness contrast may also contribute to the contrasting distribution of dyke-induced stress in the centred, strong-contact experiments (Figure 4). In both CS-1.8 and CS-0.5 the dyke remained near-vertical throughout its ascent (Figure 6C), yet the photoelastic fringes near the interface were distributed differently. In CS-1.8 ($E_U > E_L$), coloured fringes developed in both layers, but those within the stiffer upper layer were more concentrated, extended downwards along the interface and were markedly more intense than in CS-0.5 ($E_U < E_L$), in which fringes within the more compliant upper layer were weak (Figures 4B, 4C, 4E and 4F). This difference is consistent with numerical models of layered crust, in which stress concentrates preferentially in the stiffer layers (e.g., Gudmundsson, 2006; Clunes et al., 2024). In the offset experiments, by contrast, the higher-order fringes followed the dyke tip, developing within the layer through which it was propagating or which it was entering (Figure 5). Numerical models of a pressurised vertical dyke beneath a dipping, mechanically layered sequence (Clunes et al., 2023) show that vertical surface displacement becomes asymmetric when the layers are inclined and is greatest over the more compliant layer, with an asymmetry that depends on whether the inclined layer is stiffer or more compliant than the layer hosting the dyke. Those models used stiffness contrasts of 10:1 and 100:1 in both directions, much larger than those tested here, and photoelastic fringes provide only a qualitative image of the stress field, so we do not infer surface displacements from them. The experiments nevertheless show that a vertical dyke propagating beneath a dipping stiffness contrast develops a stress field whose distribution depends on which layer is stiffer, without any change in its trajectory, which is the configuration in which these models predict asymmetric surface deformation.

The PIV results document a second source of asymmetry. In OW-2A and OW-0.8, both with a weak contact, the high-strain region elongates along the upper part of the deflected dyke, and near the free surface the strain field becomes asymmetric about the vertical projection of the dyke, more markedly in OW-2A than in OW-0.8 (Figure 7). Since both dykes reach a

similar dip near the surface (Figure 6C), and the late-stage panels correspond to a similar tip depth, this difference suggests that the near-surface strain asymmetry depends not only on deflection but also on the stiffness contrast across the interface (E_U/E_L = 2 in OW-2A and 0.8 in OW-0.8). Both PIV experiments have a weak contact, so the effect of contact strength on the subsurface strain field cannot be assessed here. Together, the photoelastic and PIV observations indicate that asymmetry of the dyke-induced stress and strain fields near the surface can arise both from a stiffness contrast around a vertically propagating dyke (CS-1.8) and from dyke deflection near a weak interface (OW-2A, OW-0.8). Each configuration has been associated with asymmetric surface deformation, the first by numerical models of dipping layered sequences (Clunes et al., 2023) and the second by gelatine experiments in which a slightly inclined dyke produced asymmetric surface uplift (Kavanagh et al., 2018). Surface deformation was not analysed in this study, so whether these subsurface asymmetries produce measurably asymmetric surface signals remains to be tested.

4.2. Natural analogues: layered, folded and faulted crust

The 45°-dipping interface in our experiments represents a discontinuity that is weak in tension, such as a lithological contact or a pre-existing joint, whose resistance to opening depends on the degree of bonding across it. This resistance was controlled here through thermal welding between the gelatine layers (Kavanagh et al., 2006, 2015), which sets the fracture toughness of the interface relative to that of the gelatine (Kavanagh et al., 2017). In gelatine experiments in which the discontinuity was instead a fracture cut into homogeneous gelatine, dykes that reached the surface stopped ascending and drained into it (Le Corvec et al., 2013). In nature, magma can open such contacts, as it opens pre-existing joints, where its pressure exceeds the normal stress acting across them (Delaney et al., 1986), although intrusion along fractures oblique to the least compressive stress becomes increasingly difficult with depth, as the ambient normal stress increases (Ziv et al., 2000).

The stiffness ratios tested here (0.4–2) are modest compared with natural contrasts, since the Young's moduli of rocks commonly span two orders of magnitude and stiff lava flows may overlie soft pyroclastic layers (Gudmundsson, 2011). The effects of stiffness contrast on the induced stress field and on near-surface ascent documented here may therefore be stronger in nature, whereas the control of contact strength on deflection did not depend on

729 the direction of the stiffness contrast in our experiments. Within these limits, our results apply
730 most directly to shallow, dipping sequences of contrasting stiffness. In folded sequences,
731 such as those intruded by magmatic sheets in the Andes (González et al., 2009; Tibaldi et
732 al., 2017; Clunes et al., 2021; Martínez et al., 2023), numerical models show that
733 mechanically weak contacts rotate the local stress field and favour the deflection of sills into
734 inclined sheets, an effect that decreases as the layers steepen (Clunes et al., 2021). Our
735 experiments extend this to ascending dykes, showing that a weak contact dipping at 45° can
736 capture a dyke for stiffness contrasts in either direction, whereas a strong contact is crossed
737 without deflection but still modifies the dyke-induced stress field and the near-surface ascent
738 rate. Composite volcanoes, in which layers are commonly inclined, dipping outwards near
739 the surface and inwards at depth (Gudmundsson, 2006), and calderas, where subsidence
740 commonly tilts marginal strata towards the caldera centre (Branney, 1995; Lipman, 1997;
741 Roche et al., 2000) and ring faults can capture and deflect inclined sheets (Browning and
742 Gudmundsson, 2015), are further settings in which shallow dykes are likely to meet dipping
743 contacts of this kind.
744
745 These results lead to expectations that can be tested in eroded volcanic sequences. Dyke
746 segments that become parallel to dipping contacts should occur preferentially where the
747 contacts were poorly bonded at the time of intrusion and at shallow paleodepths, for both
748 stiffer and more compliant overlying layers, at least for the moderate contrasts tested here,
749 and the change in dip may begin before the dyke reaches the contact. Dykes meeting well-
750 bonded dipping contacts, by contrast, should maintain their path for the moderate stiffness
751 contrasts tested here, although larger contrasts may lead to arrest (Ritter et al., 2013). In
752 both cases, the interaction with the contact also modifies the induced stress field and the
753 ascent rate, which are not preserved in the rock record but are relevant to monitoring.
754
755 **4.3. Implications for volcano monitoring**
756
757 The dyke-induced stress and strain fields documented here bear on how asymmetric ground
758 deformation is interpreted during unrest. Standard dislocation models assume a
759 homogeneous elastic half-space (Okada, 1985), and models of layered volcanic crust
760 commonly assume horizontal layers (e.g., Trasatti et al., 2003; Masterlark, 2007; Bazargan
761 and Gudmundsson, 2019, 2020), so asymmetric uplift is often attributed to an asymmetric,
762 offset or dipping source. Our experiments show two ways in which the dyke-induced stress

and strain fields can become asymmetric, through a dipping stiffness contrast around a dyke that remains vertical (CS-1.8) and through deflection of the dyke near a weak dipping contact (OW-2A, OW-0.8). Only the second involves a change in the geometry of the intrusion. Numerical models predict asymmetric surface displacement for a vertical dyke beneath dipping layers, albeit for stiffness contrasts much larger than those tested here (Clunes et al., 2023). Inclined sheets also produce highly asymmetric surface displacements in horizontally layered models (Bazargan and Gudmundsson, 2020), and a slightly inclined dyke produced asymmetric uplift in homogeneous gelatine (Kavanagh et al., 2018). Asymmetric deformation alone may therefore not distinguish a vertical dyke beneath dipping heterogeneous layers from a deflected or inclined intrusion. At Tungurahua, Ecuador, weak clastic material infilling a 3-ka flank-collapse scar accounted for only ~10% of the shape of the modelled uplift, because its volume is small relative to the volume of rock through which the stress from the source passes. The asymmetric InSAR-derived inflation instead required a shallow, gently dipping source located beneath the west flank (Hickey et al., 2020). That source was inferred to exploit the collapse surface as a zone of weakness (Hickey et al., 2020), suggesting that a weak dipping discontinuity may influence where shallow magma accumulates, rather than acting only as a contrast in material properties. Whether a heterogeneity can itself produce asymmetric deformation depends on its volume and geometry relative to the source, as well as on its mechanical contrast. In our experiments, each layer occupies a large part of the volume around the dyke. Where independent constraints on layer geometry and contact properties are available, incorporating them into deformation models would help to assess whether an asymmetric signal requires an asymmetric source. Because surface deformation was not measured here, these implications remain to be tested with combined surface and subsurface measurements.

Deflection along a weak dipping contact also affects where the dyke reaches the surface. In OW-2A, OW-2B and OW-0.8, dip decreased to ~40° (OW-2A, OW-0.8) or 62–69° (OW-2B) within the uppermost few centimetres (Figure 6C), so the dyke reached the surface displaced laterally from the vertical above the injector, whereas the dykes in the strong-contact and centred experiments remained within ~12° of vertical. Lateral shifts of eruption sites have also been predicted for dykes rising through tilted lava piles, which reach the surface displaced in the dip direction of the pile rather than above the magma chamber (Gudmundsson, 2006). Similarly, numerical models of pressurised magma chambers beneath dipping layers shift the peak tensile stress at the surface, and thus the likely location

of eruptive vents, by up to ~2 km in either the up-dip or the down-dip direction (Clunes et al., 2024). Beneath calderas, unloading stresses can deflect dykes into circumferential dykes and cone sheets, with circumferential dykes erupting as short fissures outside, but parallel to, the caldera (Gaete et al., 2019). Analogue deep grabens likewise deflected dykes, which in some cases erupted outside the graben (Rahimi et al., 2025). Where shallow weak contacts dip beneath a volcano, the vertical projection of a deformation source or of the deepest seismicity may therefore not indicate where the eruption site will open, and the offset may develop only during the final stage of ascent.

The kinematic results bear on the timing of precursory signals. In the experiments in which the dyke intercepted the interface at depth, ascent rate increased from interception to eruption, to several times the rates in the lower layer in OS-0.4 and more than an order of magnitude in OW-2B. In OW-2A, the highest rates were reached only within the uppermost centimetre (Figure 6B). Because hypocentre migration is used to track dyke tips during unrest (e.g., Rivalta and Dahm, 2006), interception of a dipping contact could appear as a late acceleration in the upward migration of seismicity and in deformation rates, larger than expected from a free-surface effect alone. In OW-2B and OS-0.4 this acceleration coincided with a halt in lateral growth (Figure 6A). If a comparable halt occurs in nature, it could be expressed as seismicity that stops spreading along strike while migrating upwards more rapidly. Such signals should nevertheless be interpreted with caution. At Kilauea, only 18 of 57 eruptions and intrusions between 1960 and 1983 were preceded by an acceleration in volcano-tectonic seismicity, and these precursory sequences could not distinguish an approaching eruption from an intrusion (Bell and Kilburn, 2012). Dyke growth can also decelerate before eruption. Before the 1997 eruption at Kilauea, the rate of dyke volume change decreased with time, which was attributed to the rate of magma supply from the source rather than to propagation dynamics (Segall et al., 2001), a supply-limited regime that our constant-flux experiments cannot reproduce. At Fagradalsfjall in 2021, deformation and seismicity declined over several days before the eruption as stored tectonic stress was released, and weaker crust near the surface may have contributed to the reduced seismicity (Sigmundsson et al., 2022). This shows that crustal layering can also modify precursory signals in ways other than those documented here.

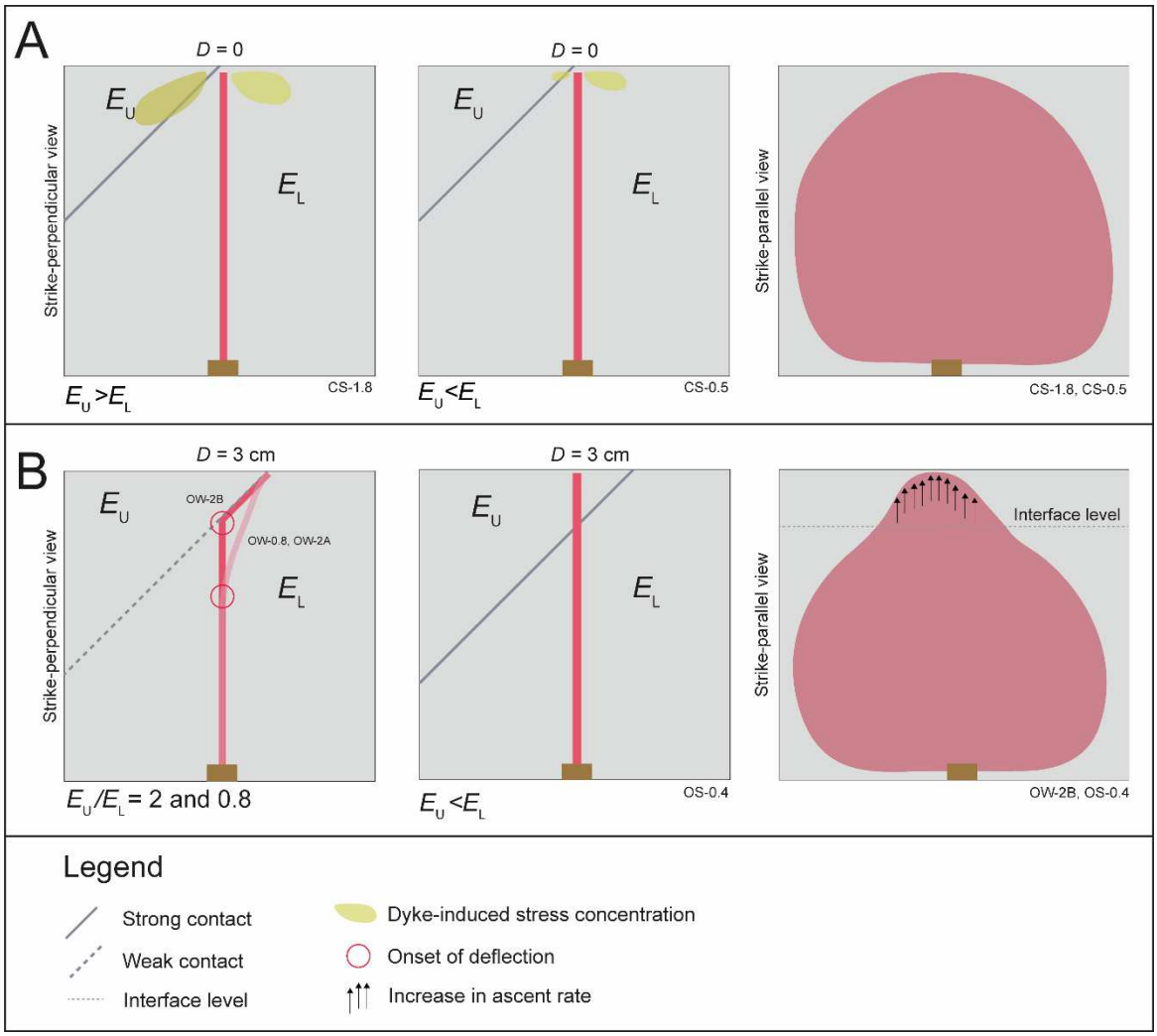


Figure 8: Schematic synthesis of the dyke–interface interactions observed in this study. (A) Centred injection (D = 0), with strike-perpendicular views of CS-1.8 ($E_U > E_L$) and CS-0.5 ($E_U < E_L$) at a late stage of ascent, and strike-parallel view of the dyke shape. (B) Offset injection (D = 3 cm), with strike-perpendicular views of the weak-contact experiments (OW-2A, OW-2B, OW-0.8) and of the strong-contact experiment OS-0.4, and strike-parallel view for OW-2B and OS-0.4.

4.4. Scope and future directions

This study was designed as a first, exploratory step towards isolating the combined and separate effects of stiffness contrast, contact strength, and the offset between the injection point and the interface on dyke-interface interaction, rather than as a fully factorial survey of these variables. Stiffness contrast, contact strength, and injection offset do not vary independently across the full set of experiments, and pairs of experiments used to isolate the effect of one variable (e.g., contact strength) are not always matched in stiffness ratio.

A fully factorial design, systematically varying all three parameters independently, would allow their combined and separate effects to be resolved with greater confidence. Interface dip itself was held constant at 45° throughout, so our results speak to the combined effect of stiffness contrast and contact strength at this single angle, rather than to how dip itself modulates these effects, a question better addressed by the numerical models discussed in Sections 4.1 and 4.2. Future experiments varying interface dip directly, complementing the numerical approach, would help establish whether the critical stiffness ratio for arrest identified for a horizontal interface (Ritter et al., 2013) shifts systematically with dip. Contact strength was also not measured directly. It was instead inferred qualitatively from the preparation temperature and visual inspection of the degree of welding between layers, rather than from an independent mechanical measurement. Kavanagh et al. (2017) derived an empirical relationship between the preparation temperature and the fracture toughness of the interface for 2.5 wt% gelatine. In addition, the transmission of shear waves across the interface, which Pansino and Taisne (2020) used to measure the stiffness of layered gelatine and expected to be inhibited by a weak interface, could provide a non-destructive measure of bonding before injection. Calibrating such measures for the gelatine concentrations used here would allow contact strength to be treated as a continuous rather than categorical variable in future studies. The orientation of the initial crack prior to injection was likewise not controlled. It deflected the dyke path in OS-1.3 and may have contributed to the slight initial inclination of the dyke in OW-2A and OW-0.8 (Section 4.1). Future experiments in which the initial crack orientation is deliberately fixed, or systematically varied, would isolate this contribution from any genuine mechanical response to the interface. The subsurface strain results are based on only two experiments, the link between interception and near-surface acceleration rests mainly on two experiments (OW-2B and OS-0.4), and the narrowing of the upper part of the dyke was documented in the two experiments with width data in which the dyke reached the interface before eruption. Expanding the dataset to include replicates of these experiments, and weak-contact experiments with stiffness ratios further below unity than OW-0.8, would allow these exploratory patterns to be tested with greater statistical confidence. Measuring surface deformation together with subsurface strain would also allow the subsurface asymmetries documented here to be linked to surface signals. Surface uplift has already been measured in gelatine dyke experiments (Kavanagh et al., 2018), and applying image correlation to the gelatine surface could provide full-field displacement maps comparable to InSAR.

5. Conclusions

We present a suite of gelatine analogue experiments in which a dyke propagates through two layers of contrasting stiffness separated by an interface dipping at 45°, an intermediate dip within the range of layer inclinations found in folded crustal sequences, composite volcanoes and caldera margins. By varying stiffness contrast and the mechanical strength of the contact between layers, and the offset between the injection point and the interface, we find that the depth at which the dyke intercepts the interface, together with the stiffness contrast across it, appears to control the near-surface ascent rate, whereas the stiffness contrast modifies the distribution of the dyke-induced stress field around a dyke that remains vertical. Contact strength, in turn, appears to control whether the dyke crosses the interface or is deflected along it. With an offset interface, a weak contact deflected the dyke for stiffness ratios both above and below unity, so that it reached the surface displaced laterally from the injection point, whereas a strong contact was crossed without deflection. This agrees with the material-toughness mechanism (Gudmundsson, 2011) if the weak contacts had a low toughness relative to that of the upper layer, which allows deflection even when the upper layer is not stiffer, and with gelatine experiments in which weak interfaces captured dykes between layers of equal stiffness (Kavanagh et al., 2017).

The experiments show that asymmetry of the dyke-induced stress and strain fields can arise in two ways. Around a dyke that remained vertical (CS-1.8 and CS-0.5), the distribution of the photoelastic fringes near the dipping interface depended on which layer was stiffer, whereas in the two PIV experiments with a weak contact (OW-2A and OW-0.8), deflection of the dyke near the interface produced near-surface strain fields that were asymmetric about the vertical projection of the dyke, more markedly for the larger stiffness contrast. Surface deformation was not analysed here, but each configuration has been associated with asymmetric surface displacement (Clunes et al., 2023; Kavanagh et al., 2018), so an asymmetric deformation signal may not by itself distinguish a vertical dyke beneath dipping heterogeneous layers from a deflected or inclined intrusion. In addition, in the two experiments with width data in which the dyke intercepted the interface well below the surface (OW-2B and OS-0.4), lateral growth almost stopped once the tip reached the interface, the upper part of the dyke narrowed into a lobe, and ascent rate increased until eruption. Because this occurred with both weak and strong contacts, with stiffness ratios on opposite sides of unity, and whether the dyke crossed the interface or was deflected along

it, it appears to be linked to the interception of the interface itself, and under the constant injection flux of our experiments the halt in lateral growth and the acceleration are likely to be two expressions of the same process. These findings should be treated as exploratory, since they are based on a small number of experiments, and the mechanical strength of the contact between layers was inferred qualitatively rather than measured directly.

These findings may be relevant to volcanic settings in which dykes propagate through dipping, mechanically heterogeneous sequences, such as folded sequences, composite volcanoes and caldera margins, and could complement deformation models that assume a homogeneous or horizontally layered crust. In such settings, a weak dipping contact may shift the eruption site laterally from the vertical projection of the source, and interception of a dipping contact could appear as a late acceleration in the upward migration of seismicity and in deformation rates. Future work should aim to replicate these results across a larger, more systematically varied set of experiments, to measure contact strength independently, to measure surface deformation together with subsurface strain, and to test whether the relationships identified here hold when interface dip itself is varied experimentally, complementing the numerical results already available for this variable.

Statements and declarations

Funding

MC acknowledges support from the ANID Scholarship Program, Beca de Doctorado Nacional 21202065, and from ANID FONDECYT Postdoctoral grant 3261114. JK acknowledges a UK Research and Innovation (UKRI) Future Leaders Fellowship (MR/S035141/1, MR/Y03418X/1). JB acknowledges FONDECYT Regular 1240188. MC also acknowledges Dawid Rybak, Zak Derler, and Kate Williams for their assistance with the experiments.

Competing Interests

Janine Kavanagh and John Browning are guest editors of the Bulletin of Volcanology special issue "Volcanic and Igneous Plumbing Systems (VIPS): Integrating Observations, Models,

and Processes". The authors have no other relevant financial or non-financial interests to disclose.

Author Contributions

MC: Conceptualization, Methodology, Investigation, Formal analysis, Software, Data curation, Visualization, Funding acquisition, Writing – original draft, Writing – review & editing. JK: Methodology, Investigation, Funding acquisition, Writing – review & editing. CC: Investigation, Formal analysis, Writing – review & editing. GA: Supervision, Writing – review & editing. JB: Methodology, Supervision, Funding acquisition, Writing – review & editing.

Data Availability

The Tracker data, the PIV data and the MATLAB scripts used to produce Figures 6, 7 and S1, together with the videos, are available in the Zenodo repository at https://doi.org/10.5281/zenodo.23701660

6. References

Bazargan, M., & Gudmundsson, A. (2019). Dyke-induced stresses and displacements in layered volcanic zones. *Journal of Volcanology and Geothermal Research*, *384*, 189-205. https://doi.org/10.1016/j.jvolgeores.2019.07.010

Bazargan, M., & Gudmundsson, A. (2020). Stresses and displacements in layered rocks induced by inclined (cone) sheets. *Journal of Volcanology and Geothermal Research*, *401*, 106965. https://doi.org/10.1016/j.jvolgeores.2020.106965

Bell, A. F., & Kilburn, C. R. (2012). Precursors to dyke-fed eruptions at basaltic volcanoes: insights from patterns of volcano-tectonic seismicity at Kilauea volcano, Hawaii. *Bulletin of volcanology*, *74*(2), 325-339. https://doi.org/10.1007/s00445-011-0519-3

Bonaccorso, A., & Davis, P. M. (1999). Models of ground deformation from vertical volcanic conduits with application to eruptions of Mount St. Helens and Mount Etna. *Journal of*

Geophysical Research: Solid Earth, *104*(B5), 10531-10542. https://doi.org/10.1029/1999JB900054

Branney, M. J. (1995). Downsag and extension at calderas: new perspectives on collapse geometries from ice-melt, mining, and volcanic subsidence. *Bulletin of Volcanology*, *57*(5), 303-318. https://doi.org/10.1007/BF00301290

Browning, J., & Gudmundsson, A. (2015). Caldera faults capture and deflect inclined sheets: an alternative mechanism of ring dyke formation. *Bulletin of Volcanology*, *77*(1), 4. https://doi.org/10.1007/s00445-014-0889-4

Clunes, M., Browning, J., Cembrano, J., Marquardt, C., & Gudmundsson, A. (2021). Crustal folds alter local stress fields as demonstrated by magma sheet—fold interactions in the Central Andes. *Earth and Planetary Science Letters*, 570, 117080. https://doi.org/10.1016/j.epsl.2021.117080

Clunes, M., Browning, J., Marquardt, C., Cortez, J., Drymoni, K., & Kavanagh, J. (2023). Inclination and heterogeneity of layered geological sequences influence dyke-induced ground deformation. *Geology*, 51(3), 278-283. https://doi.org/10.1130/G50464.1

Clunes, M., Browning, J., Cortez, J., Cembrano, J., Marquardt, C., Kavanagh, J. L., & Gudmundsson, A. (2024). Stresses induced by magma chamber pressurization altered by mechanical layering and layer dip. *Journal of Geophysical Research: Solid Earth*, *129*(5). https://doi.org/10.1029/2023JB027760

Clunes, M., Cortez, J., Ramírez, V., & Browning, J. (2026). Finite element modelling of crustal anisotropy in volcanic systems using transversely isotropic media. *Volcanica*, *9*(2), 569-585. https://doi.org/10.30909/vol/voly6220

Currenti, G., Del Negro, C., & Ganci, G. (2007). Modelling of ground deformation and gravity fields using finite element method: an application to Etna volcano. *Geophysical Journal International*, 169(2), 775-786. https://doi.org/10.1111/j.1365-246X.2007.03380.x

Delaney, P. T., Pollard, D. D., Ziony, J. I., & McKee, E. H. (1986). Field relations between dykes and joints: Emplacement processes and paleostress analysis. *Journal of Geophysical Research: Solid Earth*, *91*(B5), 4920-4938. https://doi.org/10.1029/JB091iB05p04920

Dieterich, J. H., & Decker, R. W. (1975). Finite element modeling of surface deformation associated with volcanism. *Journal of Geophysical Research*, 80(29), 4094-4102. https://doi.org/10.1029/JB080i029p04094

Feigl, K. L., Le Mével, H., Tabrez Ali, S., Córdova, L., Andersen, N. L., DeMets, C., & Singer, B. S. (2014). Rapid uplift in Laguna del Maule volcanic field of the Andean Southern Volcanic zone (Chile) 2007–2012. *Geophysical Journal International*, *196*(2), 885-901. https://doi.org/10.1093/gji/ggt438

Furst, S., Maccaferri, F., & Pinel, V. (2023). Modeling the shape and velocity of magmatic intrusions, a new numerical approach. *Journal of Geophysical Research: Solid Earth*, *128*(3), e2022JB025697. https://doi.org/10.1029/2022JB025697

Gaete, A., Kavanagh, J. L., Rivalta, E., Hazim, S. H., Walter, T. R., & Dennis, D. J. (2019). The impact of unloading stresses on post-caldera magma intrusions. *Earth and Planetary Science Letters*, *508*, 109-121. https://doi.org/10.1016/j.epsl.2018.12.016

Gaete, A., Maccaferri, F., Furst, S., & Pinel, V. (2025). Investigating the velocity of magmatic intrusions and its relation with rock fracture toughness: insights from laboratory experiments and numerical models. *Geophysical Journal International*, *240*(1), 638-651. https://doi.org/10.1093/gji/ggae396

Geshi, N., Browning, J., & Kusumoto, S. (2020). Magmatic overpressures, volatile exsolution and potential explosivity of fissure eruptions inferred via dyke aspect ratios. *Scientific reports*, *10*(1), 9406. https://doi.org/10.1038/s41598-020-66226-z

Giro, J. P., Zanella, A., Mourgues, R., Galland, O., & Ramirez, M. M. (2025). A novel adaptable analog material for simulating transversely isotropic rocks: mechanical properties and applications. *International Journal of Rock Mechanics and Mining Sciences*, *192*, 106145. https://doi.org/10.1016/j.ijrmms.2025.106145

González, G., Cembrano, J., Aron, F., Veloso, E. E., & Shyu, J. B. H. (2009). Coeval compressional deformation and volcanism in the central Andes, case studies from northern Chile (23 S–24 S). *Tectonics*, *28*(6). https://doi.org/10.1029/2009TC002538

Grosse, P., Euillades, P. A., Euillades, L. D., & Van Wyk de Vries, B. (2014). A global database of composite volcano morphometry. *Bulletin of Volcanology*, *76*(1), 784. https://doi.org/10.1007/s00445-013-0784-4

Gudmundsson, A. (2006). How local stresses control magma-chamber ruptures, dyke injections, and eruptions in composite volcanoes. *Earth-Science Reviews*, *79*(1-2), 1-31. https://doi.org/10.1016/j.earscirev.2006.06.006

Gudmundsson, A. (2011). Deflection of dykes into sills at discontinuities and magma-chamber formation. *Tectonophysics*, *500*(1-4), 50-64. https://doi.org/10.1016/j.tecto.2009.10.015

Gudmundsson, A. (2012). Strengths and strain energies of volcanic edifices: Implications for eruptions, collapse calderas, and landslides. *Natural Hazards and Earth System Sciences*, *12*(7), 2241–2258. https://doi.org/10.5194/nhess-12-2241-2012

Gudmundsson, A., Drymoni, K., Browning, J., Acocella, V., Amelung, F., Bonali, F. L., ... & Walter, T. R. (2022). Volcanotectonics: the tectonics and physics of volcanoes and their eruption mechanics. *Bulletin of Volcanology*, *84*(8), 72. https://doi.org/10.1007/s00445-022-01582-4

Hautmann, S., Gottsmann, J., Sparks, R. S. J., Mattioli, G. S., Sacks, I. S., & Strutt, M. H. (2010). Effect of mechanical heterogeneity in arc crust on volcano deformation with application to Soufrière Hills Volcano, Montserrat, West Indies. *Journal of Geophysical Research: Solid Earth*, *115*(B9).

He, M.Y., Hutchinson, J.W. (1989). Kinking of a Crack Out of an Interface. *Journal of Applied Mechanics*, 56(2): 270-278. https://doi.org/10.1115/1.3176078

Hickey, J., & Gottsmann, J. (2014). Benchmarking and developing numerical Finite Element models of volcanic deformation. *Journal of Volcanology and Geothermal Research*, *280*, 126-130. https://doi.org/10.1016/j.jvolgeores.2014.05.011

Hickey, J., Gottsmann, J., & Mothes, P. (2015). Estimating volcanic deformation source parameters with a finite element inversion: The 2001–2002 unrest at Cotopaxi volcano, Ecuador. *Journal of Geophysical Research: Solid Earth*, *120*(3), 1473-1486. https://doi.org/10.1002/2014JB011731

Hickey, J., Lloyd, R., Biggs, J., Arnold, D., Mothes, P., & Muller, C. (2020). Rapid localized flank inflation and implications for potential slope instability at Tungurahua volcano, Ecuador. *Earth and Planetary Science Letters*, *534*, 116104. https://doi.org/10.1016/j.epsl.2020.116104

Kavanagh, J. L., Menand, T., & Sparks, R. S. J. (2006). An experimental investigation of sill formation and propagation in layered elastic media. *Earth and Planetary Science Letters*, *245*(3-4), 799-813. https://doi.org/10.1016/j.epsl.2006.03.025

Kavanagh, J. L., Menand, T., & Daniels, K. A. (2013). Gelatine as a crustal analogue: Determining elastic properties for modelling magmatic intrusions. Tectonophysics, 582, 101-111. https://doi.org/10.1016/j.tecto.2012.09.032

Kavanagh, J. L., Boutelier, D., & Cruden, A. R. (2015). The mechanics of sill inception, propagation and growth: Experimental evidence for rapid reduction in magmatic overpressure. *Earth and Planetary Science Letters*, *421*, 117-128. https://doi.org/10.1016/j.epsl.2015.03.038

Kavanagh, J. L., Rogers, B. D., Boutelier, D., & Cruden, A. R. (2017). Controls on sill and dyke-sill hybrid geometry and propagation in the crust: The role of fracture toughness. *Tectonophysics*, *698*, 109-120. http://dx.doi.org/10.1016/j.tecto.2016.12.027

Kavanagh, J. L., Burns, A. J., Hazim, S. H., Wood, E. P., Martin, S. A., Hignett, S., & Dennis, D. J. (2018). Challenging dyke ascent models using novel laboratory experiments: Implications for reinterpreting evidence of magma ascent and volcanism. *Journal of*

Volcanology and Geothermal Research, *354*, 87-101. https://doi.org/10.1016/j.jvolgeores.2018.01.002

Le Corvec, N., Menand, T., & Lindsay, J. (2013). Interaction of ascending magma with pre-existing crustal fractures in monogenetic basaltic volcanism: An experimental approach. *Journal of Geophysical Research: Solid Earth*, 118(3), 968-984. https://doi.org/10.1002/jgrb.50142

Lipman, P. W. (1997). Subsidence of ash-flow calderas: relation to caldera size and magma-chamber geometry. *Bulletin of volcanology*, *59*(3), 198-218. https://doi.org/10.1007/s004450050186

Long, S. M., & Grosfils, E. B. (2009). Modeling the effect of layered volcanic material on magma reservoir failure and associated deformation, with application to Long Valley caldera, California. *Journal of Volcanology and Geothermal Research*, 186(3-4), 349-360. https://doi.org/10.1016/j.jvolgeores.2009.05.021

Maccaferri, F., Bonafede, M., & Rivalta, E. (2010). A numerical model of dyke propagation in layered elastic media. *Geophysical Journal International*, *180*(3), 1107-1123. https://doi.org/10.1111/j.1365-246X.2009.04495.x

Manconi, A., Walter, T. R., & Amelung, F. (2007). Effects of mechanical layering on volcano deformation. *Geophysical Journal International*, *170*(2), 952-958. https://doi.org/10.1111/j.1365-246X.2007.03449.x

Martínez, F., Fuentes, G., Torres, C., Peña, M., & Barraza, L. D. (2023). Emplacement and accumulation of magmatic products in contractional structures: How does it occur? Insights from Central Andes of northern Chile. *Journal of Structural Geology*, *172*, 104879. https://doi.org/10.1016/j.jsg.2023.104879

Masterlark, T. (2007). Magma intrusion and deformation predictions: Sensitivities to the Mogi assumptions. *Journal of Geophysical Research: Solid Earth*, *112*(B6). https://doi.org/10.1029/2006JB004860

Mogi, Y. (1958). Relations between the eruptions of various volcanoes and the deformations of the ground surfaces around them. *Earthq Res Inst*, *36*(99), e134.

Okada, Y. (1985). Surface deformation due to shear and tensile faults in a half-space. *Bulletin of the Seismological Society of Am*erica, *75*(4), 1135-1154.

Pansino, S., & Taisne, B. (2020). Shear wave measurements of a gelatin's young's modulus. *Frontiers in Earth Science*, *8*, 171. https://doi.org/10.3389/feart.2020.00171

Piquer, J., Skarmeta, J., & Cooke, D. R. (2015). Structural evolution of the Rio Blanco-Los Bronces District, Andes of Central Chile: controls on stratigraphy, magmatism, and mineralization. *Economic Geology*, *110*(8), 1995-2023. https://doi.org/10.2113/econgeo.110.8.1995

Rahimi, K., Bursik, M., & Kavanagh, J. L. (2025). The influence of graben geometry on dike propagation. *Journal of Volcanology and Geothermal Research*, 458, 108254. https://doi.org/10.1016/j.jvolgeores.2024.108254

Ritter, M. C., Acocella, V., Ruch, J., & Philipp, S. L. (2013). Conditions and threshold for magma transfer in the layered upper crust: Insights from experimental models. *Geophysical Research Letters*, *40*(23), 6043-6047. https://doi.org/10.1002/2013GL058199

Rivalta, E., & Dahm, T. (2006). Acceleration of buoyancy-driven fractures and magmatic dykes beneath the free surface. *Geophysical Journal International*, *166*(3), 1424-1439. https://doi.org/10.1111/j.1365-246X.2006.02962.x

Rivalta, E., Taisne, B., Bunger, A. P., & Katz, R. F. (2015). A review of mechanical models of dyke propagation: Schools of thought, results and future directions. *Tectonophysics*, 638, 1-42. https://doi.org/10.1016/j.tecto.2014.10.003

Roche, O., Druitt, T. H., & Merle, O. (2000). Experimental study of caldera formation. *Journal of Geophysical Research: Solid Earth*, *105*(B1), 395-416. https://doi.org/10.1029/1999JB900298

Rubin, A. M. (1995). Propagation of magma-filled cracks. *Annual Review Of Earth And Planetary Sciences, Volume 23, pp. 287-336.*, *23*, 287-336.

Segall, P., Cervelli, P., Owen, S., Lisowski, M., & Miklius, A. (2001). Constraints on dyke propagation from continuous GPS measurements. *Journal of Geophysical Research: Solid Earth*, *106*(B9), 19301-19317. https://doi.org/10.1029/2001JB000229

Taleghani, A. D., Gonzalez-Chavez, M., Yu, H., & Asala, H. (2018). Numerical simulation of hydraulic fracture propagation in naturally fractured formations using the cohesive zone model. *Journal of Petroleum Science and Engineering*, *165*, 42-57. https://doi.org/10.1016/j.petrol.2018.01.063

Trasatti, E., Giunchi, C., & Bonafede, M. (2003). Effects of topography and rheological layering on ground deformation in volcanic regions. *Journal of Volcanology and Geothermal Research*, *122*(1-2), 89-110. https://doi.org/10.1016/S0377-0273(02)00473-0

Segall, P. (2013). Volcano deformation and eruption forecasting. *Geological Society of London Special Publications*, 380, 85–106. https://doi.org/10.1144/SP380.4

Sigmundsson, F., Parks, M., Hooper, A., Geirsson, H., Vogfjörd, K. S., Drouin, V., ... & Ágústsdóttir, T. (2022). Deformation and seismicity decline before the 2021 Fagradalsfjall eruption. *Nature*, *609*(7927), 523-528. https://doi.org/10.1038/s41586-022-05083-4

Sparks, R. S. J. (2003). Forecasting volcanic eruptions. *Earth and Planetary Science Letters*, 210(1-2), 1-15. https://doi.org/10.1016/S0012-821X(03)00124-9

Tibaldi, A., Bonali, F. L., & Corazzato, C. (2017). Structural control on volcanoes and magma paths from local-to orogen-scale: The central Andes case. *Tectonophysics*, *699*, 16-41. https://doi.org/10.1016/j.tecto.2017.01.005

Ziv, A., Rubin, A. M., & Agnon, A. (2000). Stability of dyke intrusion along preexisting fractures. *Journal of Geophysical Research: Solid Earth*, *105*(B3), 5947-5961. https://doi.org/10.1029/1999JB900410

Supplementary Files

This is a list of supplementary files associated with this preprint. Click to download.

- ClunesetalVIPSSM.docx